UNIVERSITY OF TWENTE.

Faculty of Engineering Technology

Cooling characteristics of supercritical CO_2 flow in a tube subjected to extreme heat fluxes.

A numerical study relevant to the cooling of future nuclear fusion reactors

Henriko Schonewille

9 July 2025

Master Thesis Energy & Flow

Thermal Conversion and Storage group

Thermal and Fluid Engineering department

Daily Supervisor: Dr.Ir. A. Purandare

External Member: Dr.Ir. E. van der Weide

Chair: Prof.Dr.Ir. M. Shahi

Abstract

In this thesis, the cooling behavior of carbon dioxide in its supercritical state flowing through a tube subjected to moderate and extreme heat fluxes is numerically investigated. The extreme heat flux scenario is particularly relevant for nuclear fusion reactors, which experience heat loads on the order of 10 MW/m^2 during operation and up to 20 MW/m^2 during shut-down transients. Like many thermal systems, fusion reactors are currently cooled using water as a coolant. However, given the superior thermophysical properties of supercritical CO_2 (sCO_2) under certain conditions compared to water, and its chemical inertness, this thesis proposes sCO_2 as a potential alternative coolant. The study first examines the feasibility of simulating the so-called pseudo-boiling phenomenon, where sCO_2 transitions from a liquid-like to a gas-like state under moderate heat fluxes at supercritical pressure. This is demonstrated by qualitatively comparing simulation results with experimental and numerical data available in the literature. Subsequently, the flow of sCO_2 is simulated in a geometry specific to fusion reactors, namely a tube with an externally mounted tungsten monoblock that is exposed to extreme heat loads of 10 MW/m^2 and 20 MW/m^2. The numerical results indicate that, for similar pumping power as water, sCO_2 exhibits superior thermal performance compared to water. Specifically, the maximum temperature of the plasma facing surface of the tungsten block is significantly lower when sCO_2 is used as the coolant. This improved performance is attributed to the high heat transfer coefficients associated with pseudo-boiling transitions of sCO_2 in the flow channel beneath the heated monoblock, which is a mechanism absent in the case of single-phase water cooling. By analyzing the predicted temperature, density, and velocity profiles, further physical insights are gained into the buoyancy effects that lead to the accumulation of gas-like CO_2 near the top inner wall of the tube, which causes heat transfer deterioration for the shut-down transient of 20 MW/m^2. Recommendations are made to mitigate this effect, particularly by increasing the inlet velocity and introducing modifications to the inner surface of the tubing.

Summary

In the quest of finding a clean and sustainable energy source, nuclear fusion is considered to be a promising solution due to the abundance of available fuel and less waste than conventional power plants. In a nuclear fusion reactor, a stable plasma is created in a vacuum chamber where two hydrogen isotopes are fused together into helium, which is the same process as what is happening in the Sun and other stars. Due to the mass of the final product being lower, this releases a lot of energy. This energy can be used to create steam to turn a turbine to generate electricity, just like how it is done in conventional coal and fission power plants currently. However, nuclear fusion still faces many challenges, one of which is the cooling of the hottest component in the reactor called the divertor. The divertor is located at the bottom of the vacuum chamber, where the plasma descends during reactor shutdown, subjecting it to heat loads of up to 20 MW/m^2. Currently the divertor is made of the so-called tungsten monoblock design which is cooled using high pressure water. However, the extreme heat loads lead to cracks in the tungsten material, and the release of tungsten atoms can destabilize the plasma. In the future, fusion reactors such as ITER are expected to transition from the tungsten monoblock design to Liquid Metal Divertor (LMD) technology. This type of divertor employs a liquid metal layer on the plasma facing surface to absorb the heat loads, which then gets cooled by a coolant. However, the reactivity between water and liquid metals presents significant safety concerns, necessitating the investigation of alternative, non-reactive coolant candidates.

In this thesis, CO_2 in its supercritical state has been proposed as an alternative coolant to water. Supercritical fluids exhibit unique thermophysical properties that make them attractive for use in heat exchangers, primarily because they do not undergo a distinct phase change. When CO_2 is above its critical pressure, its behavior transitions gradually from liquid-like to gas-like as the temperature increases, which occurs over a temperature range, rather than at a single boiling point. This process is called pseudo-boiling. During this transition, properties such as density and viscosity decrease significantly, while the specific heat capacity at constant pressure c_p reaches a peak when it passes the so-called Widom-line. This sharp peak in heat capacity is one of the key reasons why sCO_2 is considered a promising alternative coolant. An additional advantage of using a supercritical fluid is the potential for Heat Transfer Enhancement (HTE). As the fluid adjacent to the heated wall increases in temperature, its density decreases, which promotes the near wall fluid to transport with the denser bulk flow away from the wall, enhancing the convective heat transfer. However, if the applied heat flux becomes excessively high, the near wall fluid may transition into a fully gas-like state, forming an insulation layer. This leads to a reduction in heat transfer performance, the so-called Heat Transfer Deterioration (HTD) phenomenon.

Initially, a feasibility study was conducted to assess the capability of simulating the coupled thermal and fluid dynamic behavior of sCO_2 within a tube subjected to moderate heat fluxes. This involved capturing the steep, non-linear variations in thermophysical properties with temperature using the commercial Multiphysics software COMSOL. The Shear Stress Transport (SST) turbulence model, most commonly used in the literature for simulating heated supercritical flows, was initially implemented. However, due to its high computational demand, the more

robust and computationally efficient k–ϵ model was adopted for the remainder of the study.

The numerical results from this feasibility study were compared against experimental and numerical data available in literature for similar geometries and operating conditions. Although notable differences were observed between the predicted and measured tube wall temperatures, largely due to insufficient mesh refinement, the overall trends in fluid temperature, density, and velocity profiles were found to be in good qualitative agreement with reference data. These findings confirmed the feasibility of simulating such problems, justifying the extension of the model for further research.

Subsequently, the same modeling approach was applied to a nuclear fusion relevant geometry involving tungsten monoblocks exposed to extreme heat fluxes of 10 MW/m^2 and 20 MW/m^2. The results demonstrated that, when using equal pumping power, supercritical CO_2 exhibited superior cooling performance compared to water. Specifically, the peak temperature of the plasma facing tungsten, was significantly lower when sCO_2 was used as the coolant. This improvement is primarily attributed to the elevated heat transfer coefficients associated with pseudo-boiling transitions of sCO_2, a mechanism absent in single phase water cooling. The findings presented in this thesis provide a solid foundation for extending the current model to future LMD concepts.

Contents

List of Figures

1 Introduction

Securing a clean, reliable, and abundant energy supply is one of humanity's most urgent and ambitious goals. While renewable energy sources such as solar and wind are making remarkable progress, their inconsistent availability limits their ability to fully meet global energy needs. Meanwhile, much of the worlds energy still depends on coal and nuclear fission technologies that raise significant concerns about sustainability, safety, and environmental impact.

In the search for a long term solution, nuclear fusion stands out as a promising alternative. By harnessing the same process that powers the stars, fusion promises an almost inexhaustible source of energy, fueled by widely available hydrogen isotopes. Over the past decades, scientific and engineering communities worldwide have been striving to unlock the potential of fusion energy, a breakthrough that could redefine the future of sustainable power generation.

The most promising concept of a nuclear fusion reactor currently is the Tokamak reactor, for which a schematic can be seen in Figure 1. In this reactor a plasma, as seen in Figure 1a, contains two isotopes of hydrogen, being deuterium and tritium, is contained in a toroidal vacuum vessel as depicted in Figure 1b and is heated to 150×10^6 degrees Celsius [9] in order for the isotopes to fuse together into helium:

$$ {}^{2}_{1}\mathrm{D} + {}^{3}_{1}\ \mathrm{T} \rightarrow {}^{4}_{2}\mathrm{He} + {}^{1}_{0}\mathrm{n} + 18\mathrm{MeV} \tag{1} $$

This process is similar to the nuclear fusion that occurs at the core of the Sun, where a tremendous amount of energy is released. The combined mass of the resulting helium nucleus and neutron is less than that of the original hydrogen isotopes. According to Einstein's mass–energy equivalence principle ($E = mc^2$), this mass loss is directly converted into energy.

In a Tokamak reactor, the plasma must be heated to temperatures nearly ten times higher than those in the core of the Sun to initiate fusion. This is necessary because, unlike in the Sun, where immense gravitational forces help overcome the electrostatic repulsion between hydrogen nuclei, fusion reactors on Earth rely solely on extreme thermal energy to bring the nuclei close enough for fusion to occur.

As previously mentioned, the plasma inside the Tokamak reactor reaches temperatures of 150×10^6 degrees Celsius, a condition that no material can withstand. To prevent the plasma from coming into contact with the reactor walls, it is confined within the vacuum chamber using strong magnetic fields, which is possible because a plasma is by definition electrically charged. This magnetic confinement ensures that the plasma remains away from the reactor walls [10]. A layout of the magnetic field coils can be seen in Figure 1. The toroidal coils produce the main magnetic field to contain the plasma and gives the plasma the doughnut-like shape. The poloidal coils help with the stability of the plasma and to keep it away from the inner wall and gives the plasma its "D" like shape. The central solenoid introduces the current in the plasma which makes it spin around the reactor to keep it stable [10].

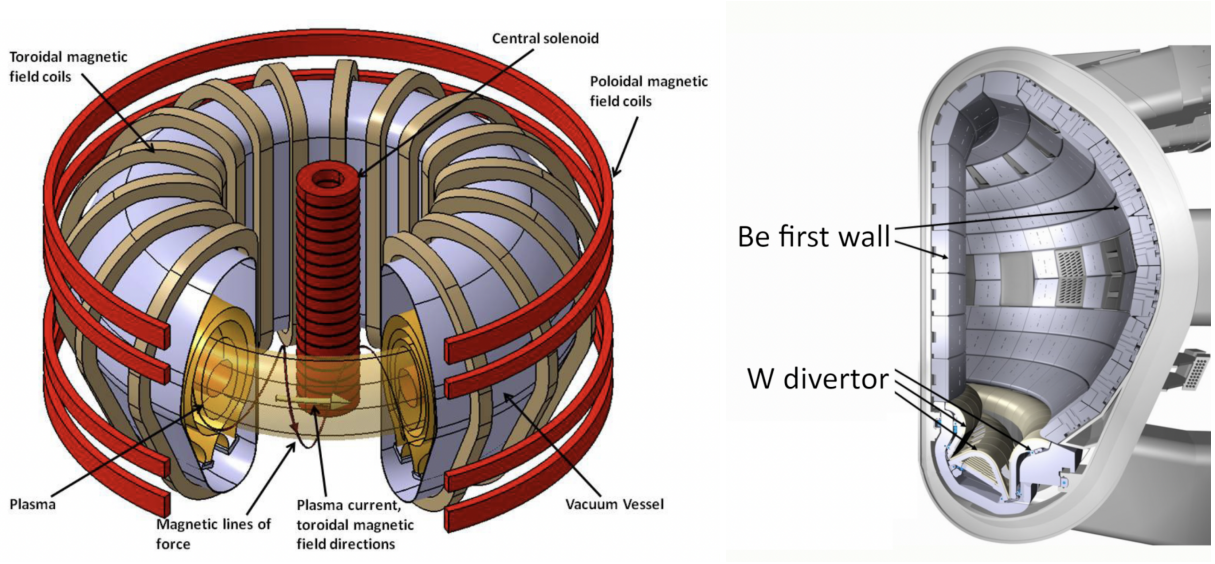

(a) Schematic of the magnetic coils

(b) Cross-section of the vacuum chamber

Figure 1: Schematic overview of a Tokamak reactor [1]

The neutrons produced during the fusion reaction (see Equation 1) are electrically neutral and therefore are not confined by the magnetic fields within the Tokamak. Instead, they travel outward and strike the beryllium (Be) first walls, where their kinetic energy is converted into heat. Approximately 80% of the energy released during fusion is carried by neutrons (14.07 MeV), while the remaining 20% is transferred to the helium nuclei (3.52 MeV) [11]. The beryllium blankets lining the reactor walls are cooled using high-pressure water systems. The absorbed heat is transferred via a heat exchanger to a lower pressure cycle, where it is used to generate steam. This steam drives a turbine to produce electricity, following a process similar to that employed in conventional coal and nuclear fission power plants.

1.1 Practicality of Nuclear Fusion Reactors

Nuclear fusion releases a lot of energy, but it also costs a lot of energy to get the fusion started and to keep the plasma stable. The fusion energy gain factor Q is introduced, which is the fusion power produced by the plasma divided by the energy used to keep the plasma stable, other energy requirements to keep the plant running are not taken into account for this value of Q. It is proven to be very hard to get a value of Q above 1 for ignition to happen. Ignition has been reached for the first time in the National Ignition Facility (NIF) in Livermore, California on December 2022, when they got 3.15 MJ of energy as output from 2.0 MJ of laser energy input ($Q = 1.575$) [12], however this laser setup is not viable to harness its energy.

The Joint European Torus (JET) which is located in Oxfordshire in the United Kingdom holds the record Q of 0.67 in a Tokamak reactor which was achieved in 1997, but this reaction was only achieved for 1 second [13, 14, 15]. The WEST Tokamak reactor located in France holds the record for longest stable plasma with a duration of 22 minutes, which was achieved in February 2025. These are promising results, but a Q higher than 5 and a pulse duration of several hours is needed for a nuclear fusion reactor to be deemed feasible.

Therefore a new Tokamak reactor is being built in southern France, being the International Thermonuclear Experimental Reactor (ITER), which is expected to be fully build by 2033/2034. The ITER will be the biggest Tokamak reactor ever build with a plasma radius of 6.2 m and a total plasma volume of 840 m^3. In comparison, the plasma volume for the JET was only 100 m^3. One of the nine parts of the vacuum chamber can be seen in Figure 2 where there can be seen how massive these pieces are when comparing it with the people walking beside it. The main goal of the ITER is to achieve a Q of 10 and a stable power generation of 500 MW [16]. The ITER is built purely for research purposes, so it will not produce electricity. The wall in the vacuum vessel is cooled by high pressure water and with the use of three heat exchanger loops the heat is dumped to the environment in the cooling tower [17, 18].

Figure 2: One out of the nine parts which will form the vacuum chamber [2].

One of the primary engineering challenges in nuclear fusion systems, next to achieving a stable plasma and a Q higher than 1, is the effective thermal management of reactor components. The divertor, located at the bottom of the reactor (see Figure 1b), is subjected to the highest thermal loads because the plasma falls in the diverter during reactor shutdown. Under normal operating conditions, the divertor is exposed to a steady-state heat flux of approximately 10 MW/m^2. However, immediately following plasma termination, this heat flux can temporarily surge to 20 MW/m^2, which is a big challenge to cool properly [19, 20, 21].

During operation the divertor catches helium ash, escaped plasma and metal atoms that came of the vessel walls [22, 23]. Therefore the divertor is sometimes also called the ashtray of the reactor. This is done by extending the magnetic field slightly on the bottom side. A schematic overview of the cross-section of the magnetic field and the divertor can be seen in Figure 3. It can be seen that there is a transition magnetic line which forms an "X" just above the divertor dome. Every atom that gets on the outside of this line will eventually reach the divertor where the vacuum pumps are installed and the debris is sucked away.

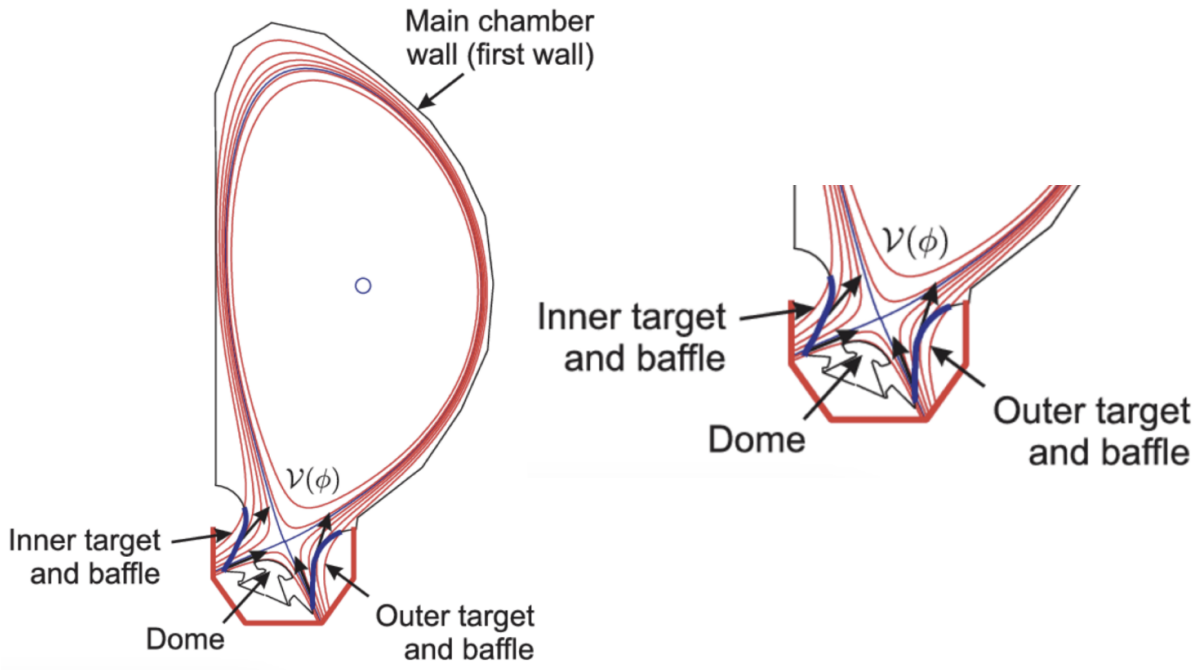

Figure 3: Schematic overview of the cross-section of the magnetic field of the reactor. [3]

Currently, the ITER divertor technology is constructed using a tungsten monoblock design, in which tungsten blocks directly face the plasma due to their high melting point and excellent resistance to sputtering. Embedded within these blocks are CuCrZr alloy pipes that circulate high pressure water to serve as the primary coolant. To facilitate efficient heat transfer and accommodate the mismatch in thermal expansion between tungsten and CuCrZr, a copper interlayer is positioned between the tungsten block and the cooling pipe. This layered configuration enhances thermal performance and structural integrity under extreme heat loads. The design of the tungsten monoblock concept is illustrated in Figure 4 and the orientation within the divertor is illustrated in Figure 5 [19, 20, 21].

The tungsten monoblock design was tested to see if it can withstand the expected heat loads in the ITER. It was found that the tungsten monoblock design can withstand a sufficient amount of steady state operation cycles of 10 MW/m^2 but that macro cracks appear at the surface of the tungsten after 500 cycles of 20 MW/m^2 [21]. The reason for these cracks is that the temperature goes above the recrystallization/creep temperature and that therefore the internal thermal stress goes beyond the yield strength of the tungsten [19]. Even though the heat transfer performance did not decrease due to the cracks, it is still not acceptable because tungsten atoms in the vacuum vessel will destabilize the plasma.

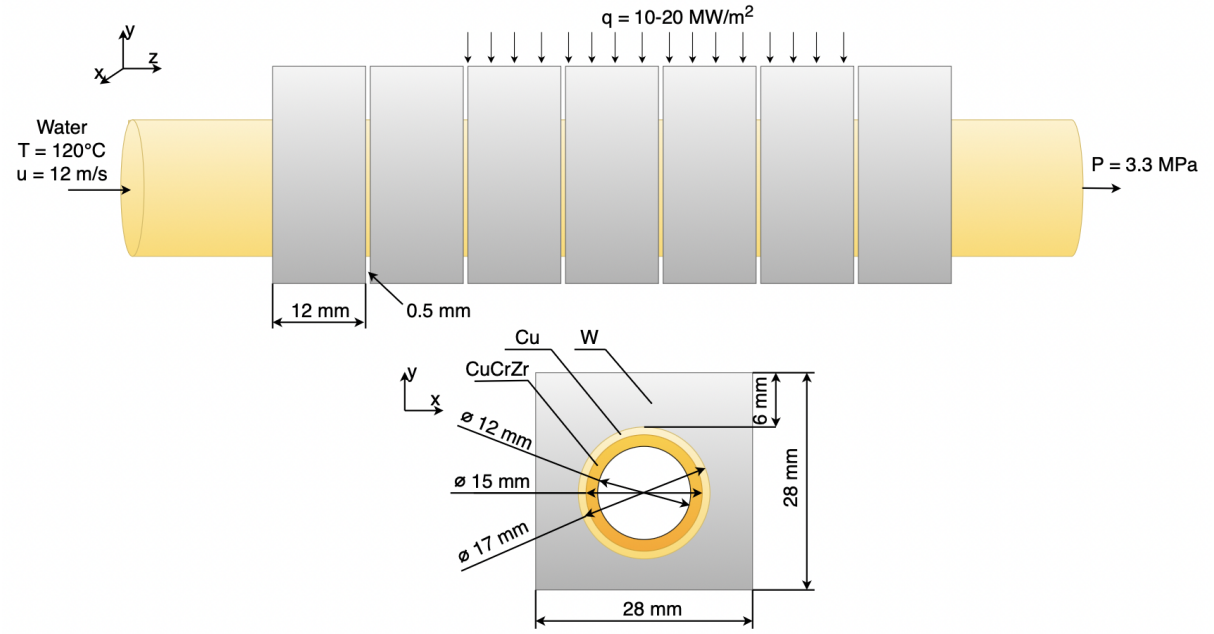

Figure 4: Schematic overview of the test set-up for the tungsten monoblock which uses water as a coolant.

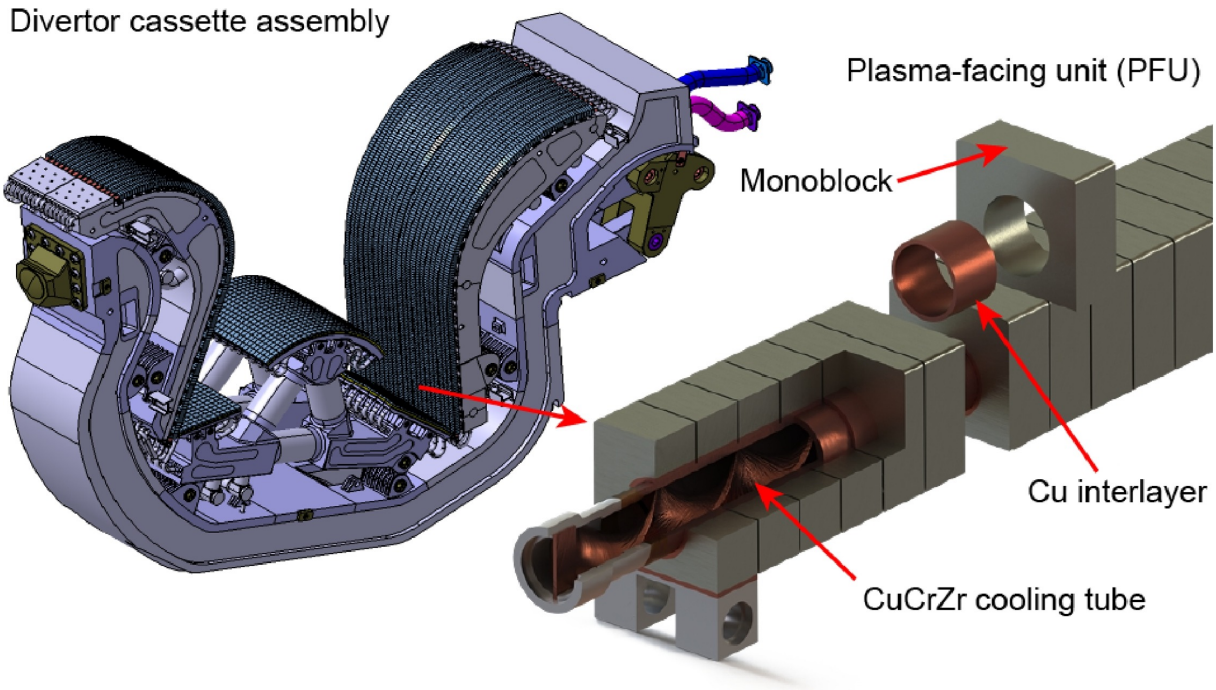

Figure 5: Orientation of the monoblock within the divertor [4].

1.2 Supercritical CO_2 as a coolant

The current tungsten monoblock divertor design employed in ITER is expected to face significant challenges in effectively managing the extreme heat fluxes, particularly in future reactors where even higher thermal loads are anticipated. As a result, advanced concepts such as the Liquid Metal Divertor (LMD) have been proposed, in which liquid metals like tin or lithium serve as

the plasma facing layer to absorb the incident heat [8]. However, due to their relatively high melting points and viscosity, these liquid metals are inefficient for long-distance heat transport, necessitating the use of an auxiliary coolant to extract and carry away the absorbed heat.

Among potential candidates, water is generally unsuitable due to safety concerns related to its reactivity with liquid metals such as lithium. Consequently, supercritical carbon dioxide (sCO_2) might be a promising alternative coolant due to its inert nature and superior thermophysical characteristics as compared to water under certain conditions. While the recent research is focused on LMD technologies, it is first essential to establish a understanding of the cooling performance of sCO_2 in conventional tungsten monoblock configurations. This thesis makes an attempt to address this gap by numerically investigating the cooling characteristics of sCO_2 under extreme heat flux conditions representative of divertor environments. The main research question is:

- Is supercritical CO_2 viable as an alternative coolant under extreme heat flux conditions representative of divertor environments?

To support the main research question of the thesis, the following sub-questions are formulated:

- What are the unique thermophysical properties of sCO_2 and how do they affect the overall heat transfer behavior?
- What are the challenges associated with modeling heated turbulent sCO_2 flows?
- How does sCO_2 compare with water under extreme heat flux conditions representative of divertor environments?

1.3 Guide through the thesis

As mentioned above, the scope of this thesis to get a better understanding for the use of sCO_2 under extreme heat flux conditions. This is done by first understanding the theoretical behavior of sCO_2 and its thermophysical properties. In the supercritical state there is no phase change which introduces unique thermophysical properties and interesting behavior due to buoyancy effects. Secondly the theory is validated in a numerical model which uses a simple horizontal pipe geometry, with a relatively low heat flux applied for which experimental data is available. It is checked if the theoretical behavior is properly modeled by comparing the outer wall temperatures between the model and the experimental data. Finally a new geometry is created which represents the set-up which is currently used for monoblock testing and the cooling performance is analyzed. The modeling software used for these tests is COMSOL v60 [24].

In **Chapter 2** a theoretical study is done. The thermophysical properties of sCO_2 are analyzed, especially near the Widom-line where the fluid transitions from liquid-like to gas-like. A comparison between these thermophysical properties of water and sCO_2 is made. Afterwards some important findings from previous studies regarding the modeling of heated sCO_2 and experimental findings are discussed. Finally an educated guess is made regarding the pumping power which is currently used for the divertor using water, and with this same pumping power the mass flux at the inlet for sCO_2 is determined.

In **Chapter 3** a feasibility study is done. An experimental test set-up of a previous study was replicated in COMSOL and the resulting outer wall temperatures of the model and the experimental data were compared with each other. The issues regarding the modeling of supercritical fluids and the reason for the choice of the $k-\epsilon$ model is explained. The behavior of the flow is discussed and compared with numerical results from previous studies.

In **Chapter 4** the monoblock model is discussed. The test set-up used in a previous experimental study is replicated in COMSOL and the maximum found surface temperatures of the plasma facing tungsten is compared. Also the overall flow behavior and regions of heat transfer enhancement and deterioration are discussed.

In **Chapter 5** a conclusion is drawn from the discussed results from the previous two chapters. In **Chapter 6** some recommendations are given for future research regarding the modeling of the tungsten monoblock, and for the Liquid-Metal-Divertor.

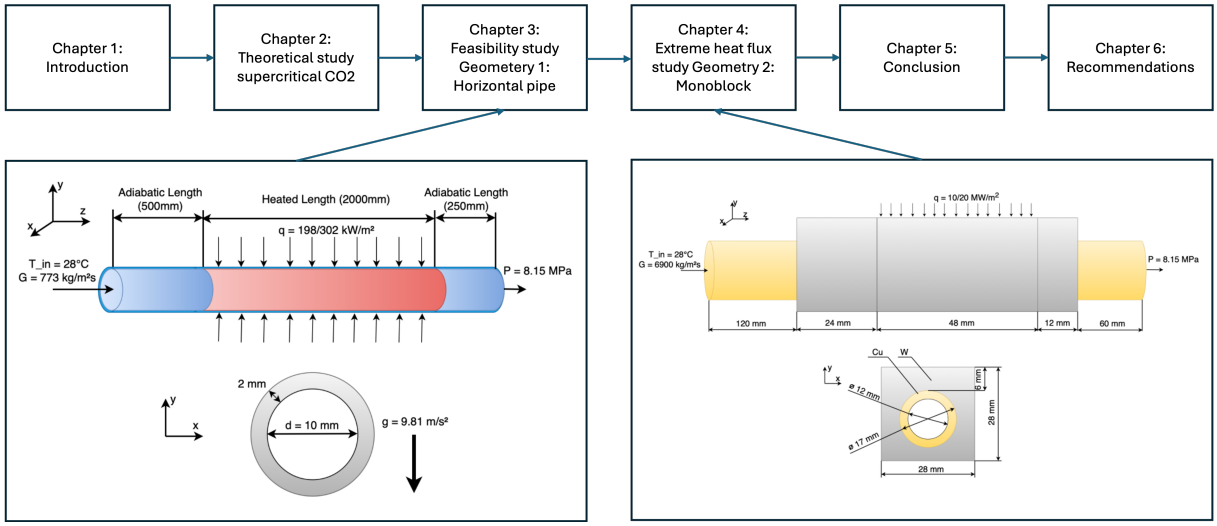

Figure 6: Flowchart of the structure of the thesis

2 Supercritical CO_2 (sCO_2)

2.1 Phase Diagram

Carbon dioxide is considered an environmentally clean and readily available fluid, which makes it an attractive candidate for use as a coolant in advanced thermal systems. Although in its liquid and gaseous states it has relatively poor thermophysical properties compared to water, the most commonly used coolant in thermal systems, it demonstrates significantly enhanced performance under certain conditions when it is in the supercritical state. CO_2 reaches its supercritical state at temperatures and pressures above its critical point (31.1 °C and 7.38 MPa), where it no longer distinguishes between liquid and gas phases.

The supercritical region can be found in the boxed of region on the top right of Figure 7. In this diagram the pressure p_r is the reduced pressure which is achieved by dividing the absolute pressure by the critical pressure. The reduced temperature T_r is found the same way by dividing the absolute temperature by the critical temperature. By doing this the critical point is located exactly at p_r and T_r equal to 1, which is marked as the magenta square in Figure 7. Using the reduced properties is useful to instantly conclude if the fluid is subcritical or supercritical.

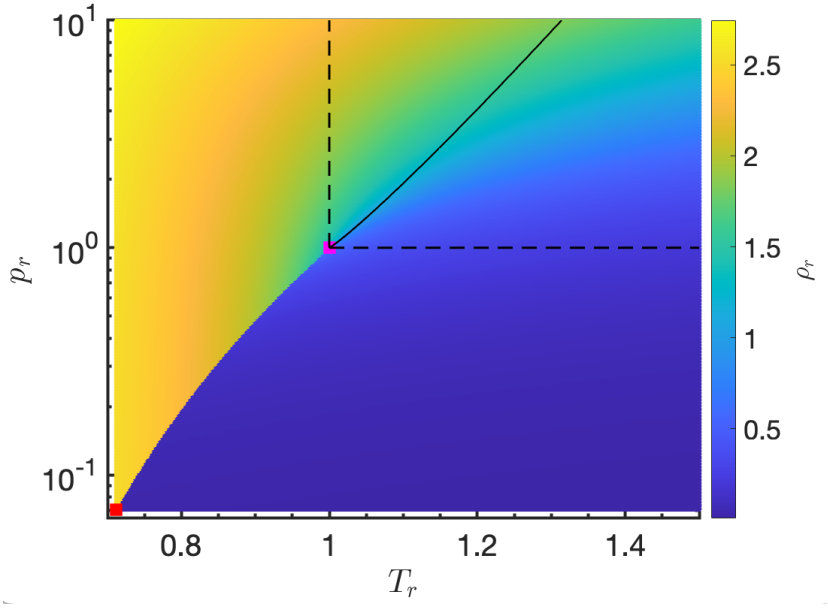

Figure 7: Phase diagram of CO_2 in reduced units, the supercritical region is in the boxed of corner on the top right.

Furthermore, the colormap presented in Figure 7 illustrates the reduced density distribution of CO_2. It can be seen via this colormap that unlike the distinct and abrupt density change observed during subcritical boiling, where liquid transitions sharply into gas, the supercritical region exhibits a more gradual and continuous variation in density. This smoother transition is separated by a characteristic boundary known as the Widom-line, shown as the solid black line in Figure 7. The Widom-line marks the location where the heat capacity peaks and serves as an extension of the liquid-gas coexistence curve into the supercritical domain [25].

The relation for this Widom-line has been approximate by NIST as a function of the reduced properties [25, 26, 27],

$$p_{\mathrm{r}} = \exp\left[A'\left(T_{\mathrm{r}} - 1\right)^{a}\right]; \quad A', a \text{ species dependent.} \tag{2}$$

where the species dependent values for CO_2 where found to be $A' = 8.256$ and $a = 1.102$ [25].

In contrast to subcritical boiling, where phase change is visible through bubble formation due to the presence of surface tension, the supercritical region lacks such clear visual indicators. As one approaches the critical point, the surface tension diminishes and eventually vanishes, making it impossible to distinguish discrete liquid and gas phases. However, a notable change in density still occurs across the Widom-line, leading to so-called pseudo-boiling, which is a transition from liquid-like CO_2 on the left of the Widom-line to gas-like CO_2 on its right. This phenomenon is of central interest in this thesis, as it is within this transition regime that supercritical CO_2 has thermophysical properties that can surpass those of water, making it a highly promising candidate for cooling applications. These advantageous properties are discussed in detail in the following subsections.

2.2 Thermophysical properties

Not only the density transitions from liquid-like to gas-like when crossing the Widom-line, it happens for several other fluid properties. This transition for the thermophysical and fluid dynamic properties relevant for this thesis is shown in Figure 8 at two different supercritical pressures evaluated using the NIST database [28, 29, 30, 31, 32, 33]. The fact there is a sharp peak in the heat capacity under constant pressure (c_p) value that far exceeds the value of water, which is around 4.2 kJ/kgK, makes sCO_2 an interesting contender for a replacement coolant, provided that the temperature of the sCO_2 can be kept close to the Widom-line. The temperature at which this peak occurs is called the pseudocritical temperature T_{pc} for that pressure. The temperature range for which sCO_2 has a higher c_p value than water is the desired operating range, which is between approximately 28 °C and 42 °C for 81.5 bar. Therefore for the rest the thesis, below 28 °C the fluid is deemed fully liquid-like and above 42 °C the fluid is fully gas-like. When comparing the c_p curves of sCO_2 for both pressures shown in Figure 8, the peak in the c_p value is significantly higher and less wide at lower pressures. This means that the operating temperature range for sCO_2 at higher supercritical pressures will be larger than for lower pressures at the cost of a lower peak in c_p.

To determine which is more desirable, the surface area under the c_p curve in the operation range for both pressures is determined, which gives the specific enthalpy. The specific enthalpy indicates how much energy can be added per kg of sCO_2 within the operating range, so a higher value is preferable. For 77.5 bar the specific enthalpy came out to be approximately 282 kJ/kg and for 81.5 bar approximately 242 kJ/kg. Therefore it can be concluded that a lower pressure, closer to the critical pressure is more desirable. However, for reasons mentioned in Chapter 3 there is still opted to continue with 81.5 bar for the rest of the thesis.

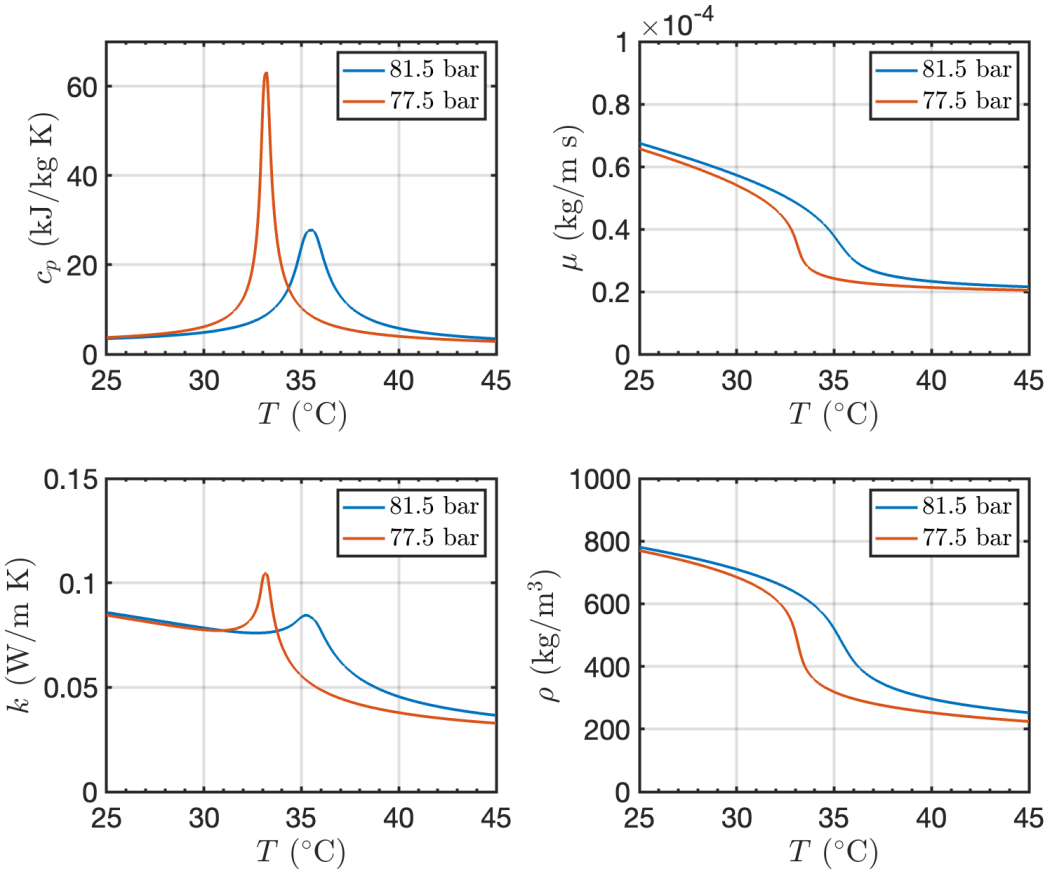

Figure 8: Thermophysical properties and fluid dynamic properties of sCO_2 at two different values of supercritical pressures.

2.3 sCO_2 versus Water

As mentioned in the introduction chapter, the current ITER monoblock design uses water as the primary coolant due to well established and studied thermal management performance. To justify the use of sCO_2 as an alternative for water as a coolant, it is essential to first compare its thermophysical and fluid dynamic properties with those of water. This comparison provides insight into the relative advantages of sCO_2 in terms of heat transfer capability, density, and viscosity under relevant operating conditions. By analyzing these differences, the motivation for exploring sCO_2 as a coolant in fusion relevant geometries becomes clearer before delving into detailed numerical simulations.

To make a good comparison between sCO_2 and water as a coolant, all of the relevant thermophysical properties are plotted against each other in Figure 9. The properties of water were taken between 120 °C and 140 °C and at a pressure of 33 bar because this is what was used in previous ITER monoblock testing [19, 34]. These properties were determined with XSteam [35]. The sCO_2 properties were taken at 81.5 bar near the Widom-line between 25 °C and 45 °C from the NIST database.

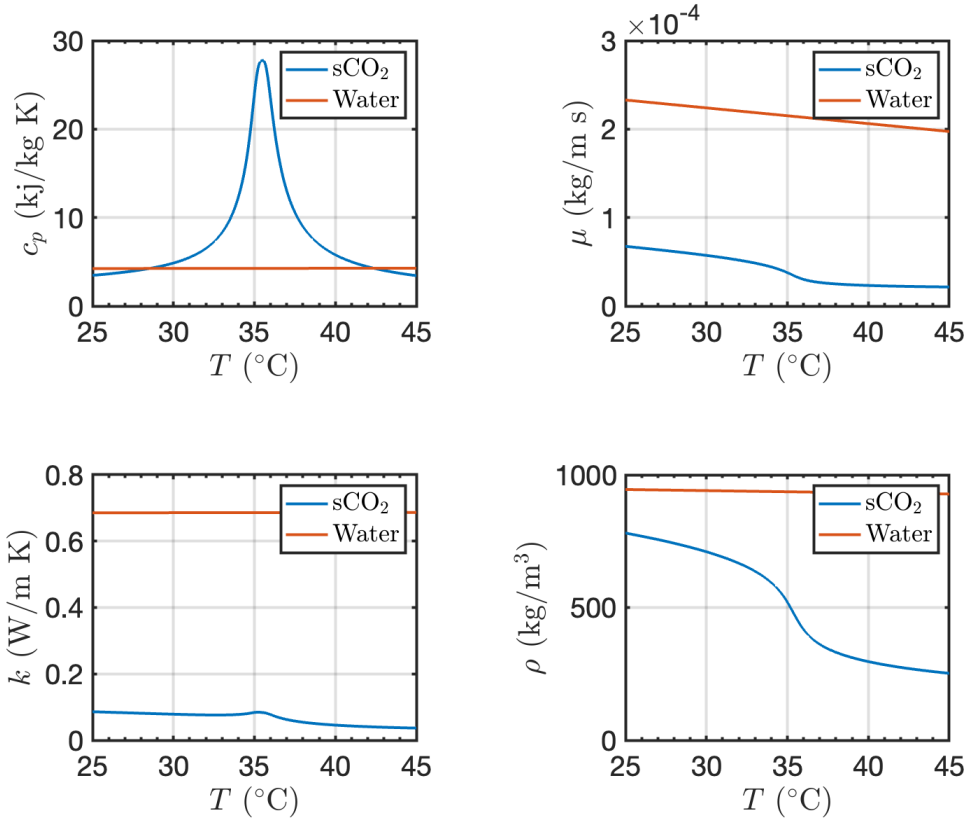

Figure 9: Thermophysical properties of sCO_2 at a pressure of 8.15 MPa versus water at 3.3 MPa.

In heat exchanger applications, desirable fluid properties are a high specific heat capacity (c_p), high density (ρ), high thermal conductivity (k), and low dynamic viscosity (μ). Between approximately 28 °C and 42 °C at a pressure of 81.5 bar, sCO_2 shows a sharp peak in c_p, reaching values significantly higher than those of water. When integrating c_p over this 14 °C range, the resulting enthalpy change for sCO_2 is approximately 242 kJ/kg. In contrast, water, with a relatively constant c_p of around 4.2 kJ/kgK, yields an enthalpy change of approximately 58.8 kJ/kg over the same temperature range, nearly four times lower.

However, water's density is also substantially higher than that of sCO_2. As illustrated in Figure 9, the average density of sCO_2 over the operating range is approximately half that of water. Consequently, while sCO_2 appears to offer approximately four times the thermal transport capacity per unit mass in this temperature window, the advantage reduces to a factor of about two when evaluated on a volumetric basis.

Also water's thermal conductivity is substantially higher than that of sCO_2. However, since a turbulent flow is considered, the conductive heat transfer is minor in comparison with the convective heat transfer. Also sCO_2 shows a significantly lower dynamic viscosity as water in Figure 9. This lower dynamic viscosity results in a lower friction in the pipes, and consequently in a lower energy loss for the same volumetric flow rate.

2.3.1 Pumping power

To make a good comparison between the cooling efficiency of sCO_2 versus water, the pumping power needed per meter is approximated which is used for ITER monoblock testing at the moment. The currently used inlet temperature is 120 °C, the inlet pressure is 3.3 MPa and the inlet velocity is 12 m/s [19, 34]. Under these conditions the density is 944 kg/m^3 and viscosity is $2.3 \cdot 10^{-4}$ kg/ms. With these properties the pumping power can be calculated using the following equation [36]:

$$P_{pump} = \frac{V\Delta P}{\eta} = \frac{V\rho g h_L}{\eta} = \frac{(vA)\rho g h_L}{\eta} = \frac{\frac{1}{4}\pi D^2 v \rho g h_L}{\eta} \tag{3}$$

where ρ is the density, g is the gravitational acceleration, V is the volumetric flow rate, η is the pump efficiency (0.75), v is the axial velocity, A is the inlet surface area and h_L is the head loss. The head loss can be calculated with the Darcy-Weisbach equation [36]:

$$h_L = f\frac{L}{D}\frac{v^2}{2g} \tag{4}$$

where L is the length of the pipe and D is the inner diameter of the pipe. The Darcy friction factor f can be approximated for turbulent flow in a smooth pipe using Blasius equation [36]:

$$f = 0.316Re^{-0.25} = 0.316\left(\frac{\rho v D}{\mu}\right)^{-0.25} \tag{5}$$

All of these equations are substituted and rewritten so that the inlet velocity can be found more easily:

$$P_{pump} = \frac{0.0395\pi D^{0.75} v^{2.75} \mu^{0.25} \rho^{0.75} L}{\eta} \tag{6}$$

Filling in this equation with L equal to 1 m, the pumping power that is used now for the ITER monoblock testing was found to be 116.8 W per meter of pipe. This power is used to calculate the conditions for sCO_2 at 8.15 MPa for both sides of the anticipated operating range. The results are displayed in Table 1. There can be seen that the pointwise mass flux for liquid-like sCO_2 is considerably higher than for gas-like sCO_2 for the same pumping power. Due to conservation of mass, the mass flux before the heated length and after the heated length need to be the same. Consequently, there can be concluded that the energy loss due to friction will be higher after the heated length, where there is assumed that the whole fluid transitioned to gas-like state. The main cause for this is the higher velocity which is needed to maintain the same mass flow due to the lower density. Next to this there is assumed that the pipe length before and after the heated part are the same, so the average of the power needed per meter between the two should be equal to 116.8 W. Using this a pointwise mass flux of approximately 6900 kg/m^{2}s was found to have the same energy loss per meter as is used at the moment for the ITER monoblock test. This pointwise mass flux is used as the inlet condition for the monoblock model and the resulting surface temperatures of the tungsten will be compared with the experimental data. The fluid at the end of the heated length might not become fully gas-like, therefore this calculated pointwise mass flux might be an under-prediction.

Table 1: Energy loss comparison between water and sCO_2.

Property	Water	sCO_2 liquid-like	sCO_2 gas-like
P_{pump} per meter	116.8 W	116.8 W	116.8 W
Pressure	3.3 MPa	8.15 MPa	8.15 MPa
Temperature	120 °C	28 °C	42 °C
Inner diameter D	0.012 m	0.012 m	0.012 m
Viscosity μ	$2.3 \cdot 10^{-4}$ kg/ms	$6.16 \cdot 10^{-5}$ kg/ms	$2.23 \cdot 10^{-5}$ kg/ms
Density ρ	944 kg/m^3	742 kg/m^3	274 kg/m^3
Axial velocity v	12 m/s	14.4 m/s	20.8 m/s
Pointwise mass flux G	11328 kg/m^{2}s	10684 kg/m^{2}s	5696 kg/m^{2}s

2.4 Heat Transfer Enhancement and Deterioration

As mentioned before, there is no phase change for supercritical fluids, therefore the heat transfer behavior is also different than for subcritical fluids. When heating a subcritical fluid, nucleate boiling happens near the heated surface and these bubbles get transported away from the wall with the bulk fluid, increasing the heat transfer. If the applied heat flux reaches the critical heat flux, these bubbles will stick to wall and a gas layer will form on the heated surface. Since the thermal conductivity of gas is lower than for liquid, it acts as an insulation layer which decreases the overall heat transfer [37].

For supercritical fluids nucleate boiling does not happen, but instead a higher temperature film will form near the wall when heated as illustrated in Figure 10. In contrary to subcritical flows, this film does not necessarily act as an insulation layer. For relatively low heat fluxes, the temperature of this film remains close to the Widom-line where the c_p value remains high and increases the overall heat transfer. This is called heat transfer enhancement (HTE). In addition, due to the absence of the surface tension between gas-like and liquid-like fluid in the supercritical region, the hotter low density fluid near the wall still mixes well with the colder high density bulk fluid. When increasing the heat flux, the layer near the wall increases in size. If this layer gets sufficiently thick, the hotter gas-like fluid directly next to the wall, with a lower c_p value, will not mix with the bulk flow, decreasing the overall heat transfer, this is called heat transfer deterioration (HTD) [5, 37].

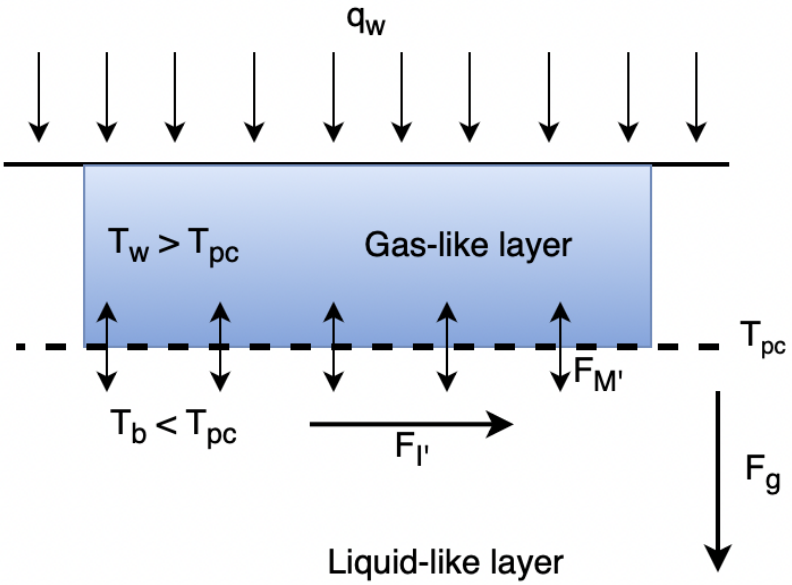

Figure 10: Schematic of the forces acting between the gas-like layer and the liquid-like bulk flow.

The two main forces responsible for the thickness of the gas-like layer near the heated surface, are the inertial force ($F_{I'}$) of the bulk liquid-like fluid and the evaporative momentum force ($F_{M'}$) as illustrated in Figure 10. If the inertial forces cannot suppress the evaporative momentum, the layer increases in thickness. Both of these forces can be determined by the following equations [37]:

$$F_{M'} = \left(\frac{q_w}{i_{fg}}\right)^2 \frac{D}{\rho_g}, \qquad F_{I'} = \frac{G^2 D}{\rho_f} \tag{7}$$

where q_w is the heat flux at the wall, D is inner diameter of the pipe, ρ_g is the density in the gas-like layer, G the point-wise mass flux, ρ_f the density of the liquid-like bulk flow and i_{fg} is the latent heat of evaporation. Even though there is no direct phase change for supercritical fluids, a latent heat is still needed to transition from liquid-like to gas-like state during pseudo-boiling, but it is over a temperature interval instead of at a set temperature [38].

2.5 Relevant Experimental Findings for Heated sCO_2 Flows

Several experiments on sCO_2 flows in a heated straight pipe geometry have previously been conducted to gain an understanding of the heat transfer and the previous mentioned phenomena. However doing so is challenging, since the velocity and temperature fields of the flow in the testing section cannot be measured directly without influencing the results, only the outer wall temperature of the testing section can be properly measured. Therefore several methods were proposed to determine if HTE or HTD is occurring, but there is no unified standard yet [39]. In this section, first one of the methods to determine if HTE or HTD occurs is described. Afterwards some results from studies are shown which derived a relation for the onset of HTD for supercritical sCO_2. Finally some other experimental findings are discussed which are relevant for the feasibility study.

For heat exchanger applications, most often the ratio between the measured heat transfer coefficient and the heat transfer coefficient calculated using the Dittus-Boelter relation is used [39]. If this ratio is greater than 1, HTE is happening and if this ratio is smaller than 1, HTD occurs. The Dittus-Boelter relation for the Nusselt number is defined as [5, 37, 40]:

$$Nu_{DB} = \frac{hD}{k_b} = 0.023 Re_{\mathrm{b}}^{0.8} Pr_{\mathrm{b}}^{0.4} \tag{8}$$

where D is the inner diameter of the pipe, k is the thermal conductivity of the fluid, Re is the Reynolds number which is the ratio of inertia forces over the viscous forces, and Pr is the Prandtl number which is the ratio of momentum diffusivity over thermal diffusivity. The subscript b indicates that these properties are taken at the bulk fluid properties. The Reynolds number and Prandtl number are defined as:

$$Re = \frac{\rho U D}{\mu}, \qquad Pr = \frac{c_p \mu}{k} \tag{9}$$

where ρ is the density, U is the velocity, D is the inner diameter of the pipe, μ is the viscosity, c_p is the heat capacity under constant pressure and k is the thermal conductivity.

The heat transfer coefficient can also be obtained with the following equation:

$$h(z) = \frac{q_{iw}}{T_{iw}(z) - T_b(z)} \tag{10}$$

where q_{iw} is the inner wall conductive heat flux from the pipe, T_{iw} is the inner wall temperature and T_b is the bulk temperature. Cheng et al. [5] used a control volume method to determine the inner wall temperature T_{iw} from the outer wall temperature measurements. For the bulk temperature, the specific bulk enthalpy i_b over the length was approximated the following way:

$$i_{\mathrm{b}}(z) = i_{\mathrm{in}} + \frac{q_{\mathrm{w}} \pi d_{\mathrm{in}} z}{\dot{m}} \tag{11}$$

where i_{in} is the specific enthalpy at the inlet, q_w is the applied heat flux, d_{in} is the inner diameter, z is the axial distance from the beginning of the heated section, and $\dot{m}$ is the mass flow rate. Since the specific enthalpy is a function of temperature and pressure, and the pressure is assumed constant, the bulk temperature distribution along the heated length can be determined directly from this specific enthalpy using the NIST database.

HTD can be detrimental for heat exchanger applications. Therefore lots of testing is carried out to evaluate the conditions at which HTD might occur. During such tests, typically the mass flux at the inlet of the heat exchanger tube is maintained constant and the heat flux is altered, and the point at which HTD occurs is recorded and is termed as the critical heat flux (q_{CHF}).

For convenience the non-dimensional number known as supercritical boiling number (SBO) is introduced, which is derived from the ratio of the previous mentioned inertial force and evaporative momentum force (see Equation 7). The SBO can be calculated as [5, 37, 41],

$$SBO = \frac{q_w}{G i_{pc}} \tag{12}$$

where q_w is the heat flux at the wall, G is the pointwise mass flux at the inlet and i_{pc} is the pseudocritical specific enthalpy. This is the specific enthalpy determined at the pseudocritical

temperature for a given pressure. Since the pseudocritical temperature increases when increasing the pressure (see the c_p graph in Figure 8), the i_{pc} also increases which would thus decrease the SBO.

Zhu et al. [37] found that an SBO exceeding approximately 5.126×10^{-4} is the onset of HTD in vertical sCO_2 pipe flows with an inner diameter of 10 mm [37]. For this thesis the pressure is taken at 81.5 bar which results in a i_{pc} of 342.55 kJ/kg, so Equation 12 can be rewritten as a relation for the critical heat flux as;

$$q_{CHF} = 5.126 \times 10^{-4} i_{pc} G = 0.176G \tag{13}$$

which shows a linear relation between the critical heat flux and the mass flux. However, another relation derived by Kim et al. [7] is also widely used in recent literature, which is given as

$$q_{CHF} = 0.0002G^2 \tag{14}$$

which shows a quadratic relation between the critical heat flux and the mass flux. This is a significant difference in findings which shows that still a lot of research is needed in this area.

Experimental data is available for both vertical and horizontal heated pipes which both give different results. The main difference between these cases is the direction of the buoyancy forces. For vertical cases, the gravity aligns with the fluid direction so the wall temperatures are the same around the circumference of the pipe when heated from all sides. For upward flows the buoyancy increases the heat transfer and for downward flows it decreases the heat transfer. For horizontal cases, especially for high SBO, the wall at the top side becomes considerably hotter than the bottom side, due to low density high temperature sCO_2 rising to the top. Due to this the gas-like layer on the top of the pipe will also become thicker than at the bottom side [5].

In the divertor technology currently present in the ITER's nuclear fusion reactor, the coolant flows both horizontally and vertically, so a choice has to be made which orientation is used for this research. One report was found that did measure the maximum temperature during these cycles, and these tests were done with a horizontal flowing high pressure water as a coolant [19, 34]. Therefore the rest of this research also focuses on horizontally orientated flows.

For the analysis of the two numerical models, which are discussed in the following chapters in the thesis, it is useful to compare the observed trends from experiments with the found trends in the numerical model. Some of the relevant experimental findings regarding horizontal heated pipes which are relevant for this research are [5, 40]:

- Heat transfer coefficient increases up until the bulk fluid reaches the pseudocritical temperature T_{pc} and then decreases further downstream.
- The temperatures of the top and bottom wall slowly start to convergence after the bulk fluid reaches pseudocritical temperature T_{pc}.
- HTE seems to happen most often when in the two-phase region near the Widom-line.

2.6 Relevant Previous Numerical Research

Numerical studies on the coupled heat transfer and turbulent flows involving supercritical fluids, particularly supercritical CO_2 , have revealed significant modeling challenges. Due to the significant property variations near the pseudocritical point, achieving accurate and reliable simulations remains difficult. Several researchers have employed various turbulence models, but differences with experimental results persist, indicating a need for further development in this area.

In the literature, three primary approaches to turbulence modeling are commonly used: Direct Numerical Simulation (DNS), Large Eddy Simulation (LES), and Reynolds-Averaged Navier–Stokes (RANS) modeling. DNS resolves all turbulent scales directly without modeling, making it the most accurate method. However, it is computationally expensive for high Reynolds number flows or large domains. LES resolves large scale turbulent structures while modeling smaller eddies, offering a compromise between accuracy and computational cost. Despite its advantages, LES remains impractical for this study due to computational limitations and available time.

As a result, this study uses a RANS-based turbulence model. Although RANS models are less accurate than DNS and LES, they are significantly more computationally efficient and are commonly used for engineering applications. They are capable of capturing general trends observed in experimental data. However, previous studies have shown that RANS models often over-predict phenomena in supercritical fluid simulations, primarily due to limitations in representing the sharp property variations. This over-prediction in the phenomena, results in an under-prediction in temperature in regions with HTE and an over-prediction in temperature in regions with HTD [42].

In previous studies involving the flow of sCO_2 though heated tubes, the solid tube was often not modeled to decrease the computational costs. The heat flux boundary condition is applied directly to the fluid domain for these studies. Xie et al. [6] conducted a numerical study with horizontal heated sCO_2 pipe flow to determine if disregarding the solid domain is a valid simplification. The results showed that this assumption was only viable for low heat fluxes cases. The deviation in wall temperatures between models including and excluding the solid wall, becomes significant when increasing the heat flux. Yang et al. [43] conducted a numerical study on the mechanisms of HTD in vertical heated sCO_2 pipe flow. They introduced a new type of HTD, being post dry-out HTD. This occurs when the bulk flow becomes fully gas-like. The results also showed that the velocity increases in this region and relaminarization happens due to the decrease in density differences. They also found that increasing the mass flux decreases post dry-out HTD, but increasing it too much prevents HTE from occurring. Buzzi et al. [44] found in a numerical study that at the beginning of the heated length the turbulence increases a lot due to buoyancy, increasing the overall heat transfer. Further downstream the density differences between the wall and the bulk flow shrink and the buoyancy induced turbulence decreases, decreasing the overall heat transfer.

From the findings from the literature, it is apparent that the buoyancy plays a key role in the heat transfer for sCO_2. Therefore it is crucial that this effect is captured in the model. To make sure this is the case, first a feasibility study was done with a different geometry, for which the wall

temperatures were compared with experimental data. The flow behavior of the feasibility study is compared with the behavior from the previous mentioned literature. This process is discussed in detail in Chapter 3. To determine if the buoyancy in the model is significant, and thus captured by the model, most often the the following buoyancy correlation is used for supercritical flows [5, 40, 45],

$$Bu = \frac{Gr_b}{Re_b^2} \tag{15}$$

where Re_b is the Reynolds number and Gr_b is the Grashof number which is the ratio of the buoyancy forces over the viscous forces. Bu is also sometimes referred to as the Richardson number, which expresses the ratio of the buoyancy term and the shear flow term. For supercritical horizontal flow it was determined that buoyancy effects are significant when Bu >0.001. The Grashof number for critical flows is often not determined with the temperature differences between the wall and the bulk flow, but with the difference in density [5, 40]:

$$Gr_{\mathrm{b}} = \frac{(\rho_{\mathrm{b}} - \rho_{\mathrm{w}})\,\rho_{\mathrm{b}} g d^3}{\mu_{\mathrm{b}}^2}, \tag{16}$$

where ρ_b is the density taken of the bulk flow, ρ_w the density taken at the wall, g the gravitational constant, d the inner diameter of the pipe and μ_b is the dynamic viscosity of the bulk flow.

3 Feasibility study: Modeling Approach and Qualitative Validation

In this chapter the feasibility of modeling the pseudo-boiling phenomenon of sCO_2 is studied. The highly non-linear variations in its thermophysical properties and fluid dynamic properties imposes numerical challenges. This study is carried out using a simplified geometric configuration for which experimental data was available.

The chapter begins by describing the geometry and boundary conditions used in the feasibility study. This is followed by an explanation of the numerical approach used to simulate the pseudo-boiling behavior of sCO_2. Finally a qualitative validation of the simulation results is presented by comparing the numerical results with experimental data, to assess the reliability and limitations of the modeling approach.

3.1 Geometry for Feasibility Study

The geometry selected for the numerical feasibility study in this thesis is based on the experimental investigation conducted by Cheng et al. [5], who studied the heat transfer characteristics of sCO_2 flowing through a heated horizontal tube. The test section from their experimental setup, which serves as the basis for the computational domain used in this study, is schematically illustrated in Figure 11. The tube is made of 1Cr18Ni9Ti stainless steel material with an inner diameter of 10 mm, an outer diameter of 14 mm and a heated length of 2 m. The inlet temperature used for the experiment is approximately 28 °C, the pressure is approximately 8.15 MPa, and the point-wise mass flux at the inlet is approximately 773 kg/m^{2}s. The heat flux on the heated part around the whole circumference is approximately 198 kW/m^2.

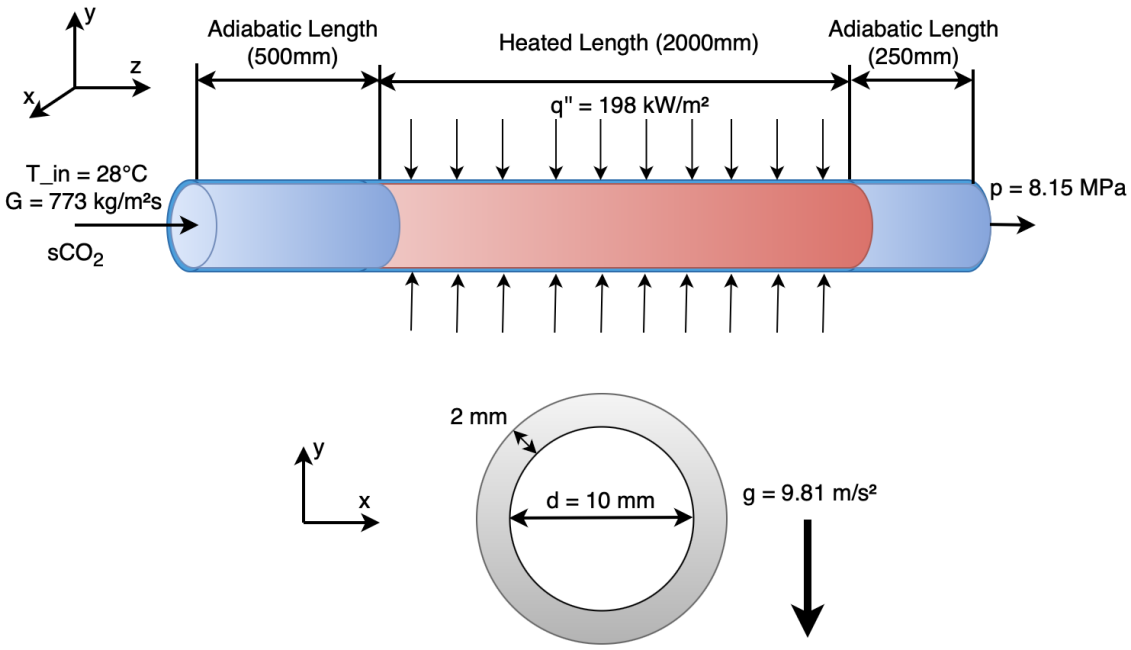

Figure 11: Schematic of the geometry and boundary conditions used to carry out the feasibility study of pseudo-boiling of sCO_2. The geometry is chosen from Cheng et al. [5].

For the computational model developed in the feasibility study presented in this chapter, the exact stainless steel alloy used for the tube material was not available in COMSOL. Therefore, standard AISI 304 stainless steel was selected as a substitute, as its thermophysical properties closely approximate those of the original alloy and are deemed sufficient for the purpose of this investigation. An adiabatic length of 0.5 m before the heated part is modeled for the flow to fully develop. An adiabatic length of 0.25 m is modeled at the end so the outlet conditions do not interfere with the test section. At the walls a no-slip boundary is applied. The overall model and its applied boundary conditions can be seen in Figure 11.

3.2 Modeling Approach

In the numerical model, coupled heat and momentum transport phenomenon associated with the pseudo-boiling of sCO_2 is investigated under steady-state conditions using the previously defined geometry. The density, velocity, and temperature fields are computed numerically using the Finite Element Method (FEM). These simulations are carried out using the commercial software package COMSOL Multiphysics [24]. The details of the numerical model are presented in this section.

3.2.1 Treatment of sCO_2 Properties

The properties of sCO_2 are not directly available in COMSOL. In the COMSOL literature, the adopted approach to determine the thermophysical properties of fluids in the supercritical region involves the use of the Peng–Robinson equation of state with a high-pressure viscosity correction [46]. The resulting thermophysical and fluid dynamic properties obtained through this method after manual implementation inside COMSOL are compared with the corresponding properties of sCO_2 extracted from the standard NIST database [28, 29, 30, 31, 32, 33] for three different supercritical pressures, as illustrated in Figure 12. The properties of COMSOL only align when farther away from the Widom-line and COMSOL does not recognize that there should be a peak in thermal conductivity near the Widom-line. Since the desired operation range is near the Widom-line these properties will not be acceptable to use.

Because of the limitations associated with using the Peng-Robinson equation of state for the thermophysical properties of sCO_2, an alternative approach was adopted for this study by utilizing data from the NIST database. For the four relevant properties displayed in Figure 12, 5000 data points in the anticipated temperature range were extracted and directly implemented into COMSOL as material property inputs. Within COMSOL, linear interpolation is performed between successive data points. When a sufficient large number of points is used, this interpolation provides a reasonably accurate approximation of the actual property variations with temperature, as illustrated for example for c_p in Figure 13. Outside of the anticipated temperature range, COMSOL sets a constant value of the property as indicated by the red dashed line in Figure 13.

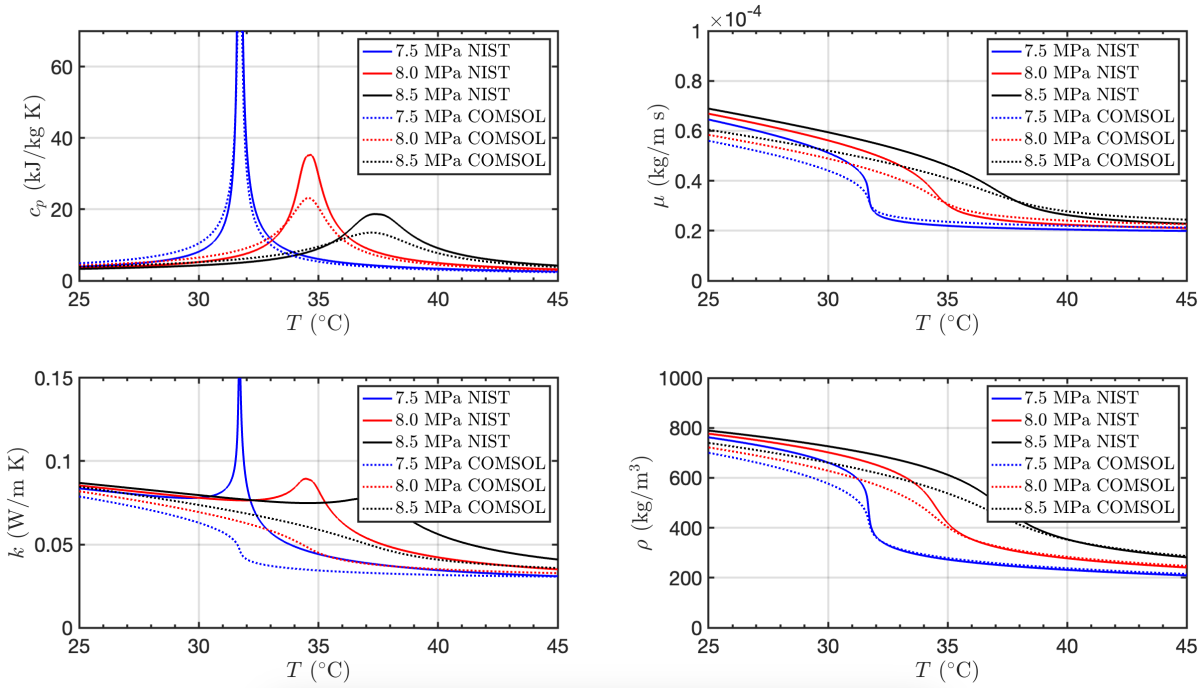

Figure 12: Comparison between the Thermophysical and fluid dynamic properties of sCO_2 determined using Peng-Robinson EOS with that of NIST database for different supercritical pressures at the crossover of the Widom-line.

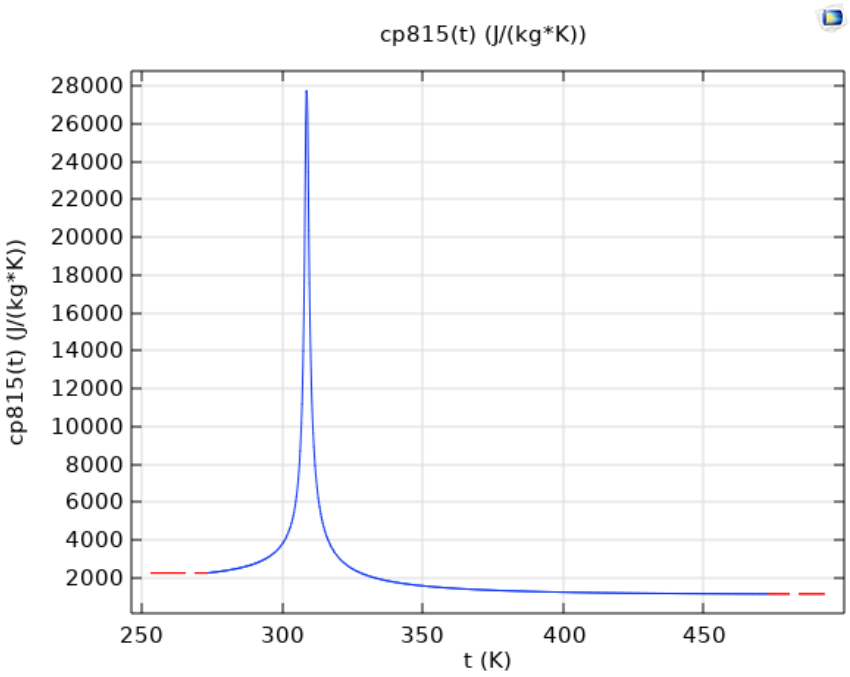

Figure 13: Interpolated values of c_p of the anticipated temperature range of the research taken from COMSOL. Outside of the anticipated temperature range constant values are chosen.

3.2.2 Governing Equations

The governing equations in the solid tube domain is the heat equation:

$$\rho c_p \frac{\partial T}{\partial t} - k \frac{\partial T}{\partial x_i} = 0 \tag{17}$$

where ρ is the density, c_p is the heat capacity, k is the thermal conductivity, and T is the temperature.

The governing equations for the sCO_2 fluid domain are the RANS equations. These are obtained by first dividing the flow quantities into an average part and a fluctuating part like the velocity for example:

$$u_i = \bar{u_i} + u_i' \tag{18}$$

where u_i is the actual velocity, $\bar{u}$ is the average velocity and u' is the fluctuating part of the velocity. By inserting this relation for all the primitive variables into the conservation of mass, momentum and energy equations, the RANS equations are obtained [6, 47, 48]:

$$\frac{\partial \rho}{\partial t} + \frac{\partial}{\partial x_i}(\rho u_i) = 0 \tag{19}$$

$$\frac{\partial}{\partial t}(\rho u_i) + \frac{\partial}{\partial x_j}(\rho u_i u_j) = -\frac{\partial p}{\partial x_i} + \frac{\partial}{\partial x_j}\left[\mu\left(\frac{\partial u_i}{\partial x_j} + \frac{\partial u_j}{\partial x_i} - \frac{2}{3}\delta_{ij}\frac{\partial u_k}{\partial x_k}\right) - \rho\overline{u_i' u_j'}\right] + \rho g \tag{20}$$

$$\frac{\partial}{\partial t}(\rho H) + \frac{\partial}{\partial x_i}(\rho u_i H) = \frac{\partial}{\partial x_i}\left(\frac{\lambda}{c_p}\frac{\partial H}{\partial x_i} - \rho\overline{u_i' H'}\right) \tag{21}$$

where ρ is the density, u_i is the velocity in direction i, p is the pressure, μ is the dynamic viscosity, g is the gravitational constant, H is the enthalpy, λ is the thermal conductivity, and c_p is the heat capacity under constant pressure. The term δ_{ij} is the Kronecker delta which is equal to 1 when $i = j$ and 0 when $i \neq j$, $\rho\overline{u_i' u_j'}$ is the Reynolds stress tensor, and $\rho\overline{u_i' H'}$ is the turbulent heat flux term. The bar on top of these last two mentioned terms indicates that it is the Reynolds averaged term. Both terms are calculated for a compressible flow using Boussinesq approximation as follows [48, 49]

$$-\rho\overline{u_i' u_j'} = \mu_t\left(\frac{\partial u_i}{\partial x_j} + \frac{\partial u_j}{\partial x_i} - \frac{2}{3}\frac{\partial u_k}{\partial x_k}\delta_{ij}\right) - \frac{2}{3}\rho k\delta_{ij}, \qquad -\rho\overline{u_i' H'} = \frac{\mu_t}{\mathrm{Pr}_t}\frac{\partial H}{\partial x_i} \tag{22}$$

where μ_t is the turbulent eddy viscosity and Pr_t is the turbulent Prandtl number which is often set at 0.85, but for buoyancy driven turbulent flows for supercritical fluids, a lower value might give better results [42, 50]. How the turbulent eddy viscosity is determined is dependent on the turbulence model used. Two different turbulence models were considered, being the SST k-ω model and the $k - \epsilon$ model.

3.2.2.1 SST Turbulence Model and Wall Functions

Most computational studies on the modeling of turbulent sCO_2 use a SST k-ω turbulence model because it perfectly combines the high precision of a $k-\omega$ model near walls and the high precision of $k-\epsilon$ in the free stream, so it describes the pseudo-boiling near the wall very well [6, 43, 45, 51, 52]. The SST model is a two equation model which calculates the turbulent eddy viscosity with the turbulent kinetic energy k and the turbulent specific rate of dissipation ω. With a certain complicated blending function the $k-\omega$ model transitions to a $k-\epsilon$ model when moving away from the wall, for which the total derivation can be found in the COMSOL manual [53]. The two model equations are:

$$\rho\frac{\partial k}{\partial t}+\frac{\partial}{\partial x_i}\left(\rho u_i k\right)=\frac{\partial}{\partial x_j}\left[\left(\mu+\frac{\mu_t}{\sigma_k}\right)\frac{\partial k}{\partial x_j}\right]+G_k-Y_k \tag{23}$$

$$\rho\frac{\partial \omega}{\partial t}+\frac{\partial}{\partial x_i}\left(\rho u_i \omega\right)=\frac{\partial}{\partial x_j}\left[\left(\mu+\frac{\mu_t}{\sigma_\omega}\right)\frac{\partial \omega}{\partial x_j}\right]+G_\omega-Y_\omega+D_\omega \tag{24}$$

where σ_k and σ_ω are turbulent Prandtl numbers which connect the diffusivity of k and ω to the eddy viscosity, which are set as 0.81 and 0.5 respectively. G_k and G_ω are production terms and Y_k and Y_ω are dissipation terms [6]. Since in the end this turbulence model will not be used, it will not be discussed in more detail in this report, the full terms can be found in the COMSOL manual [53].

The reason this model was not used for this research, is because the y^+ value of the first cell near the wall needs to be lower than 1. If y^+ is higher than 1 wall functions will be used by COMSOL instead, so all the advantages of using the SST model vanishes. The y^+ value is defined as

$$y^+=\frac{yu_\tau}{\nu}=\frac{yu_\tau\rho}{\mu}, \qquad u_\tau=\sqrt{\tau_w/\rho} \tag{25}$$

where y is the distance from the center of the cell to the wall, ν is the kinematic viscosity, μ is the dynamic viscosity, ρ is the density and τ_w is the wall shear stress. The wall shear stress can be calculated with the following equation:

$$\tau_w=\frac{1}{2}f_f\rho U^2 \tag{26}$$

where U is the free stream velocity and f is the Fanning friction factor. For turbulent flow in a smooth pipe this can be approximated by Blasius equation as:

$$f_f=0.079Re^{-0.25} \tag{27}$$

Note that this is a different friction factor as used in Chapter 2.3.1, the Fanning friction factor is four times as small as the Darcy friction factor.

The value required for y to reach $y^+=1$ is calculated for both the liquid-like properties and gas-like properties taken from Table 1 and the results can be seen in Table 2. For the prism layers at the boundary, the first layer thickness is set at 0.0014 mm with 25 total layers and a growth factor of 1.25 is chosen. Next to this it is important that the free stream elements are

of approximately the same size as the last boundary layer element for stability and accuracy reasons [54]. By doing this the total amount of elements is approximately 8.15 million when using tetrahedral elements, generating a mesh of this size with quadrilateral elements made COMSOL crash every time.

Table 2: First cell thickness calculations to reach $y^+ = 1$

Property	sCO_2 liquid-like	sCO_2 gas-like
Pointwise mass flux G	773 kg/m^{2}s	773 kg/m^{2}s
Free stream velocity U	1.04 m/s	2.82 m/s
Reynolds number	125272	346493
Friction factor f_f	0.0042	0.0033
Wall shear stress τ_w	1.69 N/m^2	3.60 N/m^2
First cell center distance y	1.74 $\cdot 10^{-6}$ m	7.1 $\cdot 10^{-7}$m
First layer thickness	0.0035 mm	0.0014 mm

The papers of previous research used a quadrilateral mesh to achieve $y^+ = 1$ with an amount of cells ranging from around 4 million to 5 million cells for models which are approximately the same size [6, 43, 45, 51, 52]. With the available computational resources a mesh with approximately only 1.5 million quadrilateral elements, including prism layers, was solvable before running out of memory. Such a mesh had a y^+ value of approximately 15. When using the default tetrahedral elements, less than 5 million elements can be used before running into memory problems. For this mesh the y^+ value was still approximately 10. Both of these meshes were impossible to convergence.

Because the y^+ value was too high, COMSOL automatically uses wall functions instead. The wall functions are plotted next to the actual dimensionless velocity profile ($u^+ = U/u_\tau$) in Figure 14. Up until y^+ 5 the viscous sub layer is located where the velocity profile can be approximated by $u^+ = y^+$. From y^+ 30 and higher the Log-law region is located, for which the velocity profile can be approximated by the following equation:

$$u^+ = \frac{1}{\kappa_v} log(y^+) + B$$

where κ_v is the Von Kármán constant which is 0.41 and B is an empirical constant which is set as 5.2 in COMSOL. In between y^+ 5 and 30 there is no proper function to describe the profile. For this reason this so-called buffer layer should be avoided [55]. This does not only apply to the velocity but also for the temperature and the turbulent kinetic energy for which the buffer zone is also between y^+ 5 and 30. As mentioned before, when trying to use the SST turbulence model the y^+ values were approximately 10-15, so within this buffer layer. This also contributed to the convergence issues next to the extreme non-linear sCO_2 properties.

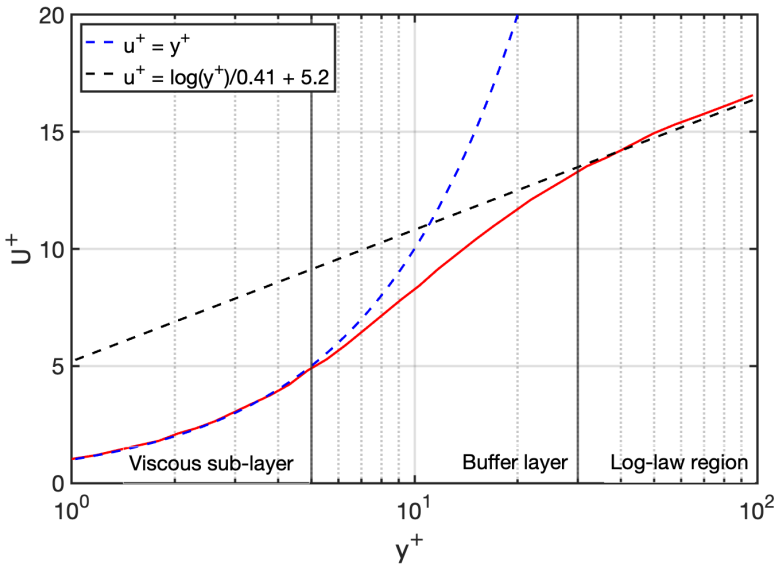

Figure 14: The wall functions used in COMSOL next to the actual velocity profile which is plotted in red

3.2.2.2 K-Epsilon Turbulence Model

Since a finer mesh is not possible due to the available computational resources and the available time, a $k-\epsilon$ model was used, which utilizes wall functions. To ensure the log-law wall function is applicable, the mesh was designed to achieve y^+ values within the 30-100 range. To achieve this, the boundary layer prism elements were omitted and a pure tetrahedral mesh was created. While accurate resolution of the near-wall region is critical for capturing the pseudo-boiling effect, the removal of prism layers was necessary to ensure numerical convergence and enable progress in the study.

For the $k-\epsilon$ model the turbulent eddy viscosity is defined as:

$$\mu_t = \rho C_\mu \frac{k^2}{\epsilon} \tag{28}$$

Where C_μ is a constant which is empirical derived to be 0.09, k is the turbulent kinetic energy and ϵ is the turbulent dissipation rate. The values for k and ϵ are determined from the following two equations [49, 56, 57]:

$$\underbrace{\frac{\partial}{\partial t}(\rho k)}_{\text{Rate of increase}} + \underbrace{\frac{\partial}{\partial x_i}(\rho k u_i)}_{\text{Convective transport}} = \underbrace{\frac{\partial}{\partial x_j}\left[\left(\mu + \frac{\mu_t}{\sigma_k}\right)\frac{\partial k}{\partial x_j}\right]}_{\text{Diffusive transport}} + \underbrace{P_k}_{\text{Rate of production}} - \underbrace{\rho\epsilon}_{\text{Rate of destruction}} \tag{29}$$

$$\underbrace{\frac{\partial}{\partial t}(\rho \epsilon)}_{\text{Rate of increase}} + \underbrace{\frac{\partial}{\partial x_i}(\rho \epsilon u_i)}_{\text{Convective transport}} = \underbrace{\frac{\partial}{\partial x_j}\left[\left(\mu + \frac{\mu_t}{\sigma_\epsilon}\right)\frac{\partial \epsilon}{\partial x_j}\right]}_{\text{Diffusive transport}} + \underbrace{C_{1\epsilon}\frac{\epsilon}{k}P_k}_{\text{Rate of production}} - \underbrace{C_{2\epsilon}\rho\frac{\epsilon^2}{k}}_{\text{Rate of destruction}} \tag{30}$$

where σ_k and σ_ϵ are turbulent Prandtl numbers which connect the diffusivity of k and ϵ to the eddy viscosity, which are set at 1.0 and 1.3 respectively. $C_{1\epsilon}$ is an empirical derived constant which tunes the production of ϵ which is set at 1.44 and $C_{2\epsilon}$ tunes the destruction of ϵ which is set at 1.92. P_k is a production term that for a compressible flow is often given as [57, 58]

$$\begin{aligned} P_k &= \tau_{ij}\frac{\partial u_i}{\partial x_j} \\ \tau_{ij} &= \mu_t\left(2S_{ij} - \frac{2}{3}\frac{\partial u_k}{\partial x_k}\delta_{ij}\right) - \frac{2}{3}\rho k\delta_{ij} \\ S_{ij} &= \frac{1}{2}\left(\frac{\partial u_i}{\partial x_j} + \frac{\partial u_j}{\partial x_i}\right) \end{aligned} \tag{31}$$

where τ_{ij} is the Boussinesq approximation of the Reynolds stress tensor and S_{ij} is the strain rate tensor.

3.2.3 Numerical Solver

The Generalized Minimal Residual Method (GMRES) solver is used which is an iterative solver which is the default solver for COMSOL. An iterative solver is chosen because it performs better than a direct solver for larger models with a lot of elements [59]. Next to this a segregated solver is chosen which solves the primitive variables separate from the turbulence variables. The primitive variables are the velocity field (u, v, w), pressure p and temperatures T. The turbulence variables are the turbulent kinetic energy k and the turbulent dissipation rate ϵ or the specific dissipation rate ω, depending on the turbulence model used. Convergence is reached when the error estimates for both groups reaches below 10^{-4}. The other settings were left as default.

3.2.4 Numerical Stability

Due to the highly non-linear properties a lot of convergence and stability issues arose, especially for lower pressures near the supercritical point and for cases with high SBO, so more buoyancy induced turbulence. In order to combat this these properties are ramped up starting from a linear relation all the way up to actual material properties. A parameter called xyz is used for this which ranges from 0 to 1 (0 0.2 0.4 0.6 0.8 0.9 0.95 1). For every xyz step, the previous solution is used as an initial condition to help with convergence. If these step sizes happen to be too large, COMSOL automatically takes a smaller step size (smallest possible step 0.01) to help with convergence. The equations used for the ramping of the thermophysical properties at 8.15 MPa can be seen in Equation 32 and are visualized in Figure 15.

$$\begin{aligned} c_p &= (1 - xyz)\cdot 12000 + xyz \cdot c_p815(T), \qquad \rho = (1 - xyz)\cdot 500 + xyz \cdot \rho815(T) \\ \mu &= (1 - xyz)\cdot 4 * 10^{-3} + xyz \cdot \mu815(T), \qquad k = (1 - xyz)\cdot 0.06 + xyz \cdot k815(T) \end{aligned} \tag{32}$$

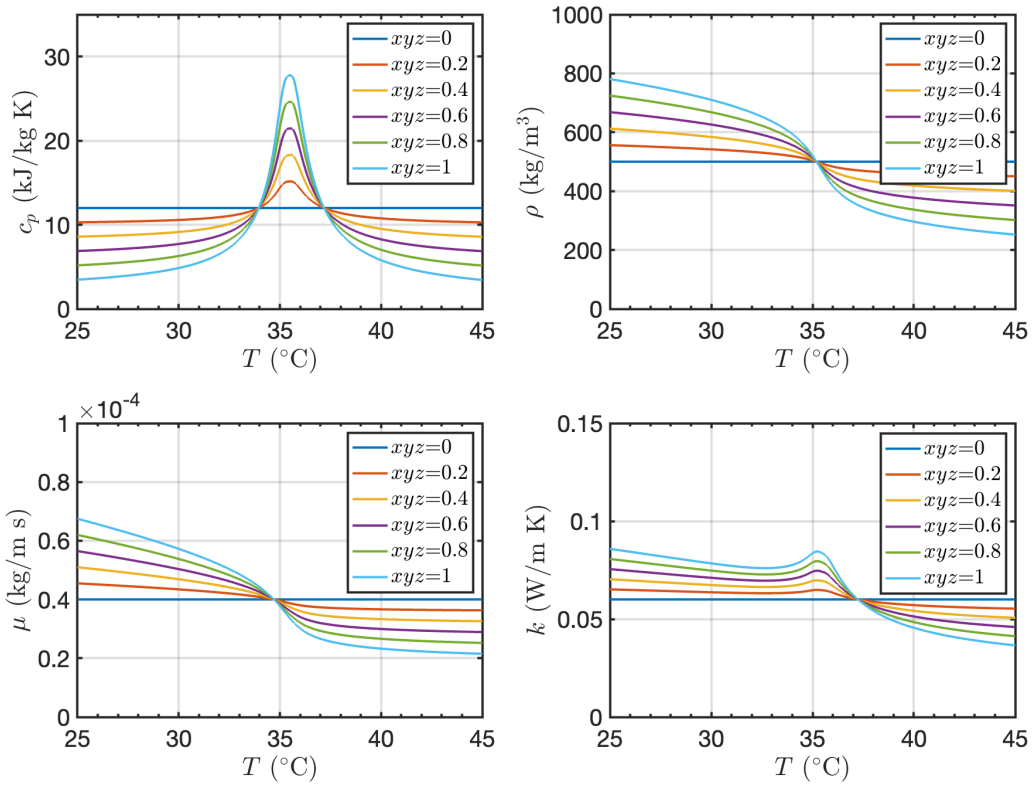

Figure 15: Property scaling for used pressure of 8.15 MPa which is used to help with numerical stability and convergence

Even with this property ramping convergence was still hard to achieve. Some settings were tried out that were recommended by COMSOL to try to improve the convergence. These findings are summarized in Table 3. A default tetrahedral mesh is used over a quadrilateral mesh for this research. A disadvantage of using tetrahedral elements for CFD is that elements do not align as good as quadrilateral elements to the flow so more numerical diffusion occurs [60]. Due to this numerical diffusion, the steep gradients in thermophysical properties smoothen out, which is most probably the reason the tetrahedral mesh did converge better.

3.3 Results of Feasibility Study

Given the exceptionally large geometry selected for the feasibility study (2.75 meters in length and 10 mm in diameter as described in Section 3.1), achieving a grid independent solution for simulating the pseudo-boiling phenomenon exceeded the practical time limits of this thesis, since the simulations required several weeks of computational time. Even a grid comprising of approximately 5 million elements, which was approximately the available memory limit for this research, was not grid independent yet as described in more detail in Appendix A. Consequently, this section presents a qualitative comparison between the experimental findings of Cheng et al. [5] and the numerical results obtained in this study and those reported by Xie et al. [6].

Table 3: COMSOL settings tested to improve convergence

Difference from default	Convergence effect	Remarks
Using another iterative solver as the default GMRES	No effect	Seems to have no effect for convergence
Adaptive mesh	Small improvement	Refines the mesh in regions with steep gradients and coarsens other regions for every ramping step, runs into memory problems because all meshes have to be stored to be able to use previous solution.
Quadratic turbulence elements	Small improvement	Big increase in memory use but less fine mesh is needed for same accuracy
Quadratic temperature elements	No effect	Big increase in memory use and computational time
Adaptive mesh and quadratic turbulence elements	-	Memory problems already for extremely coarse mesh and during the first steps of ramping
Isotropic diffusion	Big improvement	Solution converges very easily but results are very inaccurate and unusable (top and bottom wall temperatures are exactly the same)
Quadrilateral mesh	Slightly worse	Takes very long to generate in comparison with the default tetrahedral mesh, higher memory cost but less fine mesh needed for same accuracy, cells are better aligned with flow direction so less numerical diffusion
Transient model	-	Transient model proved really hard to set up for such a large model because initial values need to be really good approximated
Remove boundary prism layers	Big improvement	Less accuracy near wall, big improvement in convergence

3.3.1 Qualitative Comparison with Experimental Results

As illustrated in Figure 16, it can be seen that the outer wall temperatures predicted by the present numerical model do not quantitatively match with the experimental data reported by Cheng et al. [5]. However, the overall trends show reasonable qualitative agreement. Specifically, both the simulated and measured results exhibit an increasing trend in wall temperature along the length of the heated tube, with the top wall temperature consistently higher than the bottom wall temperature. Additionally, the temperature difference between the top and bottom walls is more pronounced near the entrance of the heated section and gradually decreases downstream. For a grid independent solution this temperature difference is assumed to be greater and more in line with the experimental data as described in Appendix A. The larger initial difference can be attributed to the region where the bulk fluid temperature approaches the pseudocritical temperature T_{pc}. Beyond this point, the top and bottom wall temperature converge as the influence of pseudo-boiling weakens along the tube length.

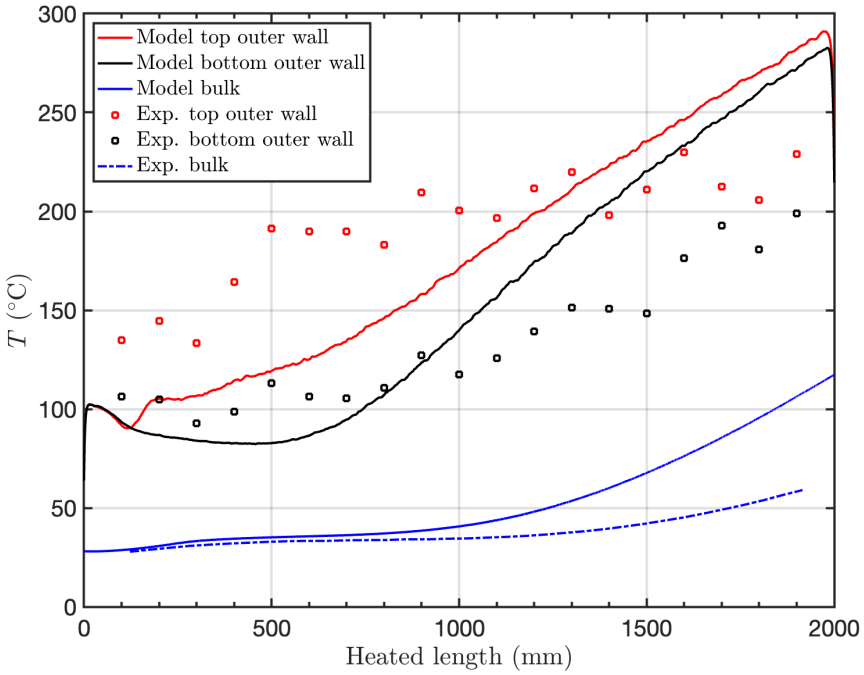

Figure 16: Comparison of measured [5] and numerically predicted temperature profiles along the length of the heated tube, showing the outer wall temperatures (top and bottom) and bulk fluid temperature of sCO_2. (p = 8.15 MPa ; q"= 198 kW/m^2; G=773 kg/m^{2}s)

To explain these previous mentioned findings, first the buoyancy number Bu is plotted over the heated length as can be seen in Figure 17. The buoyancy effects increase just at the start of the heated length and decrease further downstream. The buoyancy number in the second half goes below 0.001 which means that the buoyancy effect is negligible [40]. The reason for this is that the fluid is fully in gas-like state and the density differences are not as large anymore. Due to this decrease in buoyancy, the heat transfer decreases as well, explaining the raise in wall temperatures downstream. The other relevant dimensionless numbers needed to determine the buoyancy number, can be found in Appendix C.

The fact that the turbulence decreases for the second half can also be concluded when looking at the longitudinal velocity contour and its streamlines in Figure 18, for which the y-scale has been increases by a factor 50 (just like the rest of the longitudinal figures in this section) for increased visibility. The streamlines mix up at the start of the heated length, but become parallel again in the second half. This is the so-called relaminarization or post-dryout HTD which was also found in previous studies [44, 43]. It can also be seen that the velocity magnitude increases at the end of the heated length. This behavior can be attributed to the decrease in fluid density in this region. Due to the principle of mass conservation, the mass flux must remain constant along the flow direction, thus increasing the velocity.

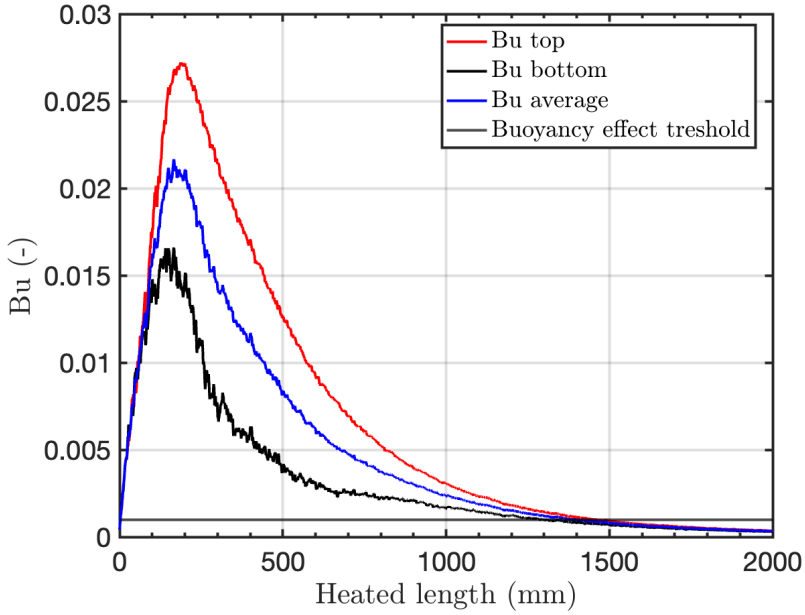

Figure 17: Buoyancy number over the heated length

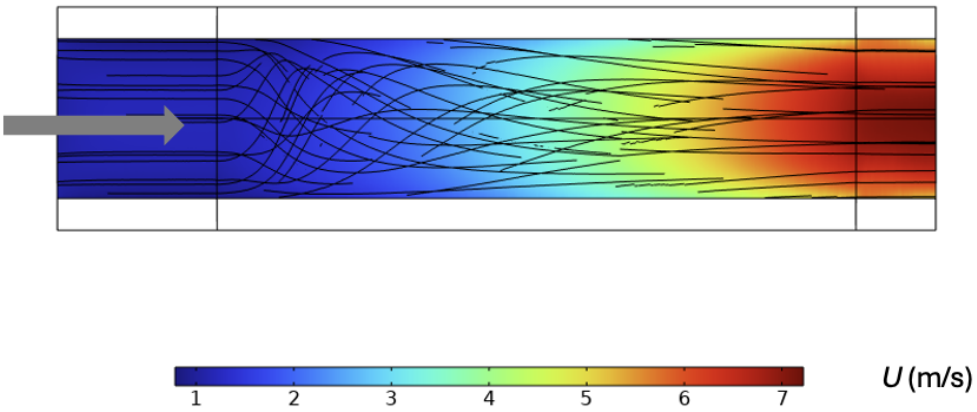

Figure 18: Velocity field and flow streamlines for sCO_2 flow through a heated tube. The vertical lines on the left and right side indicate the start and end of the heated portion of the tube, respectively.

The longitudinal temperature contour can be seen in Figure 19. The color scale is chosen so that the fully liquid-like region (below 28 °C) is dark blue and the fully gas-like region (above 42 °C) is dark red, with the pseudocritical temperature of 35 °C in the middle in white. It can be seen that the top side crosses the Widom-line further upstream than the bottom side. It can also be seen that after around halfway of the heated length, all of the fluid is in the gas-like state. Due to the fluid being in the same state, the buoyancy decreases again as was also concluded when looking at the Bu number. In this plot the color scale was capped at 42 °C but the actual maximum temperature at the outlet was higher at approximately 150 °C.

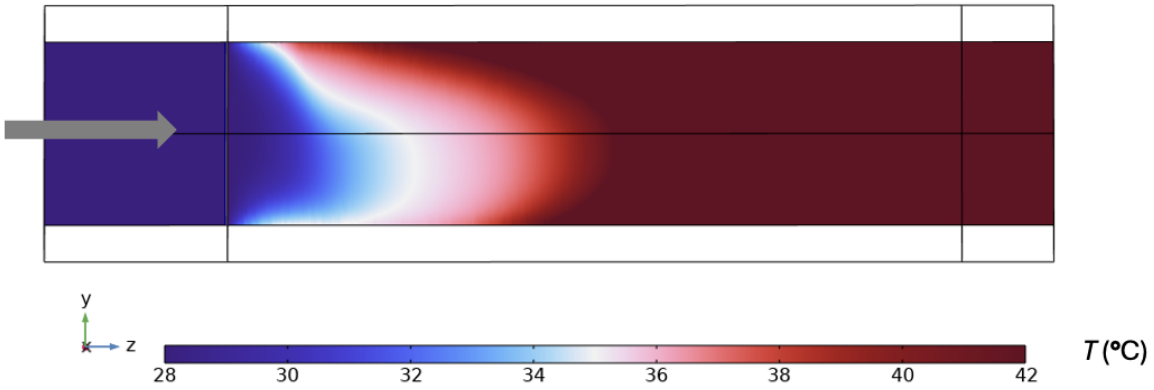

Figure 19: Temperature field of sCO_2 flowing through a heated horizontal tube. Color blue corresponds to liquid-like sCO_2 and red indicates gas-like sCO_2, reflecting the pseudo-boiling transition along the longitudinal direction.

3.3.2 Qualitative Comparison with Numerical Results

This section presents and discusses the results of various parameters along the longitudinal and radial directions of the heated tube, where the supercritical fluid undergoes pseudo-boiling. Longitudinal contours of the heated length of other relevant properties are shown in Figure 20, where they are compared with results from Xie et al. [6]. For this research the heated length was 1640 mm, so the contours are also taken over the same distance instead of entire length of the tube geometry. For these results they used sCO_2 at 7.75 MPa with an inlet temperature of 20°C and a pointwise mass flux of 400 kg/m^{2}s. The heat flux at the boundary was 90 kW/m^2 and the inner diameter was also slightly smaller at 8 mm. They also had the computational resources to use the SST turbulence model. Even though all of the boundary conditions and turbulence model were different for this research, these results are still useful to qualitatively compare with the results of the numerical model developed in this research.

Similar contour trends are observed when comparing the present results (left column) with the numerical results from Xie et al. [6] (right column) in Figure 20. It can be seen that the temperatures rise near the walls at the end, primarily at the top wall for both studies. It can also be seen that the density drops rapidly at the start of the heated length, and that this drop is sharper at the top side of the flow. The density contour of both studies look similar to the temperature field shown in Figure 19, which is to be expected since the density is only a function

of temperature for this case. From the c_p plots, it can be seen that for both studies a curve with increased values is present, which is where the Widom-line is located. This same curve is also visible for the thermal conductivity plots, however the value increase is less significant. Next to this it can be seen that the thermal conductivity first slowly decreases downstream, then slowly increases and then rapidly decreases for both studies.

Next to similarities also a few difference are spotted. The main difference is that for this study the Widom-line is found further upstream. This can be attributed to the fact that a higher heat flux was applied for this study and thus an earlier transition to the gas-like phase happens. Another difference is that the values of primarily c_p are significantly lower, this is due to the fact that for this study a higher pressure is used which means a lower peak in the heat capacity (see also Figure 8).

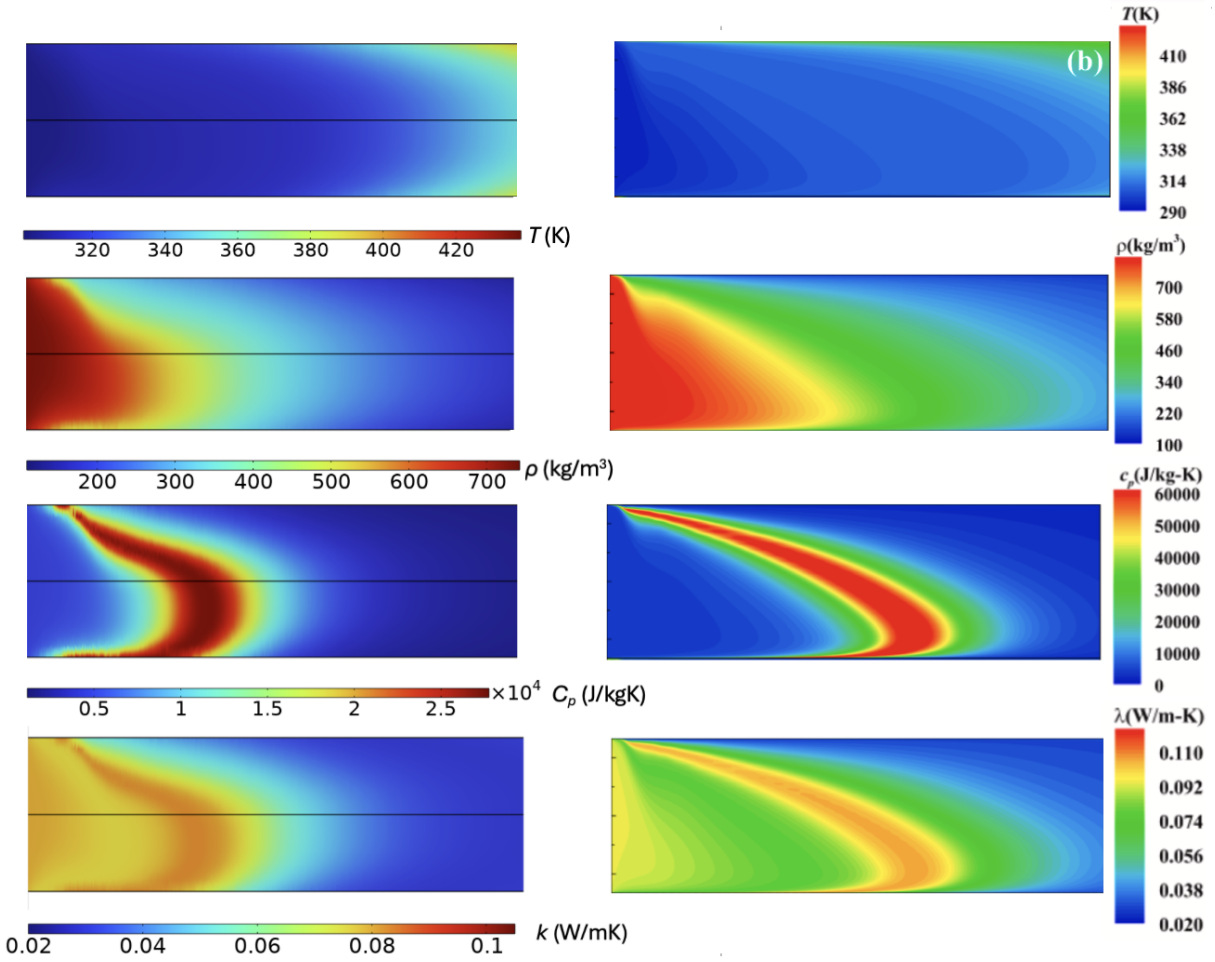

Figure 20: Qualitative comparison between the numerical results of the current study (left column; p=8.15 MPa, q"=198 kW/m^2 and G=773 kg/m^{2}s) with the numerical results from [6] (right column; p=7.75 MPa, q"=90 kW/m^2 and G=400 kg/m^{2}s) in the longitudinal direction. The flow direction is from left to right.

In addition to the longitudinal contours also the results in the radial direction are compared with the results of Xie et al. [6] as seen in Figure 21. All of these cross-section results are taken at the point where the effect of buoyancy was the highest, so at approximately 0.2 m into the heated length. The radial velocity magnitude ($\sqrt{u^2 + v^2}$) and the corresponding streamlines are included to illustrate the influence of buoyancy on the flow field. Additionally, the fluid density distribution is shown, as it plays a crucial role in driving buoyancy effects under supercritical conditions.

The radial velocity and its streamlines are shown on the left in Figure 21. It can be seen that fluid rises up near the walls and circulates back down in the middle of the pipe, which happens for both studies. The main difference between the models is that the circulation area is closer to the wall in case of the results from Xie et al. [6]. This is attributed to the finer mesh and the better near wall accuracy from the SST turbulence model. On the right hand side the density profiles are shown. For both studies the density on the topside is lower. Also the density closer to the walls is lower than the middle in all directions, but the gradients are steeper from Xie et al. [6]. In case of the density profile from Xie et al. [6], a characteristic U-shaped low-density region is observed at the top. This is only faintly visible in the density results predicted from the present model, likely due to the coarser mesh resolution and differences in the turbulence modeling approach.

3.4 Concluding remarks for feasibility study

Overall it can be concluded that the modeling approach employed for this thesis, which utilizes the standard k-ϵ RANS turbulence model, is a feasible method for obtaining engineering level estimates of pseudo-boiling behavior in sCO_2. The simulation results showed reasonable qualitative agreement with both the experimental observation from Cheng et al. [5] and the numerical findings from Xie et al. [6]. The absolute values are slightly off, but the overall flow and thermal trends were captured correctly, all though in a lower resolution. The model captured key characteristics of the pseudo-boiling regime, including the occurrence of HTE in the initial heated section and HTD in the later stages of the heated length, which is in line with the previous mentioned literature.

Based on these observation, the modeling approach was deemed suitable for further application. The same approach is employed for a tungsten monoblock geometry with extreme heat loads applied relevant to nuclear fusion applications. These heat loads are two orders of magnitude higher than those considered in this chapter and no previous studies were available which considered heat loads of this magnitude. The results of these simulations are presented and discussed in the following chapter.

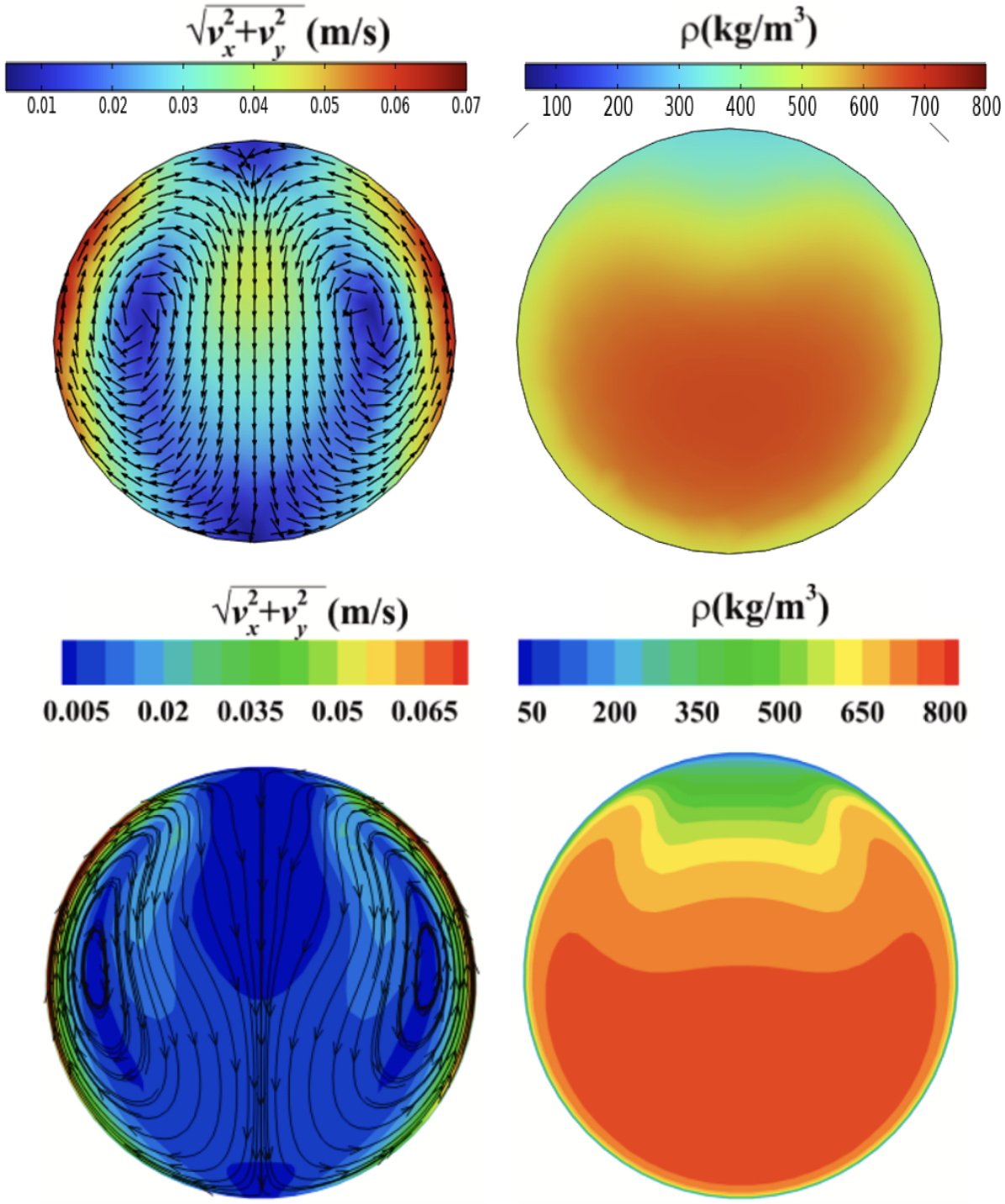

Figure 21: Qualitative comparison between the numerical results of the current study (top row; p = 8.15 MPa, q"= 198 kW/m^2 and G=773 kg/m^{2}s) with the numerical results from [6] (bottom row; p = 7.75 MPa, q"=90 kW/m^2 and G=400 kg/m^{2}s) in the radial direction at the location with highest buoyancy effect.

4 Viability of sCO_2 as a Coolant for Fusion Reactors

After motivating the use sCO_2 as a coolant in Chapter 2, and the demonstrating the feasibility of numerically modeling the coupled heat and momentum transport involving sCO_2 undergoing pseudo-boiling in Chapter 3 , this chapter focuses on the numerical investigation of the cooling performance of sCO_2 in a nuclear fusion context. Specifically, the analysis targets the thermal management of the ITER divertor, which employs tungsten monoblocks (as illustrated in Figure 4) and is subjected to extreme heat fluxes expected during fusion plasma operation. The study aims to assess the effectiveness of sCO_2 in mitigating these heat loads and to provide insights into its thermal behavior under such demanding conditions.

4.1 Tungsten Monoblock

The current divertor design employed in the ITER fusion reactor is based on a tungsten monoblock configuration. This design comprises a series of solid tungsten blocks mounted on a copper cooling pipe, which facilitates heat removal from the plasma-facing surface of the monoblocks. For this thesis, a further simplified geometry is adopted, as illustrated in Figure 22. Specifically, the 0.5 mm gap between adjacent tungsten blocks is neglected to avoid the need for excessively fine mesh resolution in those regions. This is undesirable for the fluid domain because the mesh keeps on getting finer and coarser when passing through every monoblock. This gave complications regarding the y^+ value, which was tried to keep around 30-300 so the log-law wall function could be used again. Removing these gaps should not make significant change to the maximum surface temperature in the tungsten because there is no convection in between these gaps during the experiments. Additionally, the CuCrZr cooling pipe and the copper interlayer, originally two distinct components in Figure 4, are here represented as a single domain, due to their comparable thermophysical properties. Before entering the monoblock an adiabatic pipe length of 10 times the inner diameter is modelled for the flow to develop and an adiabatic pipe length of 5 times the inner diameter is modelled so that the outlet conditions do not interfere with the heated part, and so that the flow after the monoblock also could be analyzed. A surface heat flux boundary condition of 10 and 20 MW/m^2 is applied to the top face of the central tungsten monoblock, consistent with the heating area used in the experimental setup described by Hirai et al. [19]. All other external surfaces are assumed to be adiabatic.

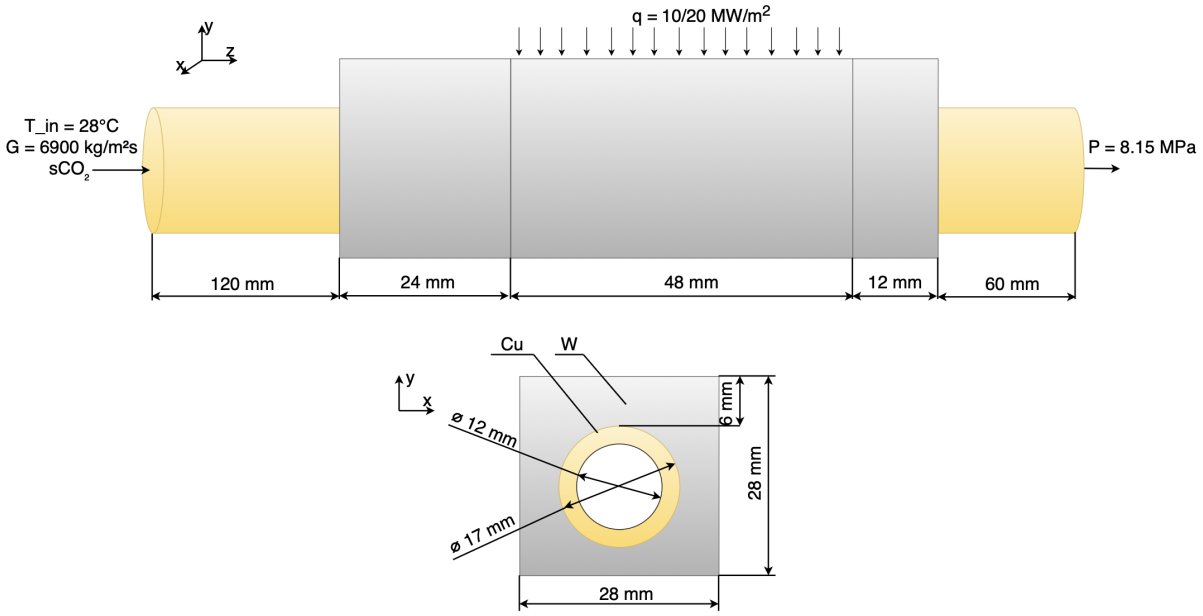

Figure 22: Schematic overview of the computational domain and the boundary conditions used to study the cooling behavior of sCO_2 flow through tungsten monoblock.

The modeling approach and governing equations outlined in Section 3.2 are directly applied to the tungsten monoblock geometry considered in this chapter. The main difference is that for the tungsten monoblock a time-dependent study is carried out instead of a stationary study, so the unsteady terms of the equations also needed to be resolved. A time-dependent numerical study is employed to maintain consistency with the experimental work presented by Hirai et al. [19], in which the heat loads were applied in pulsed time intervals. The monoblock was modeled for a time span of 40 seconds and the heat flux was applied in pulses of 10 seconds with 10 seconds downtime in between. Only the second cycle will be analyzed because the first cycle includes initial transient effects during the experiments which were not visible for the subsequent cycles [19]. For the time discretization an implicit scheme is used because of the relatively long time span of the simulation. Implicit schemes are unconditionally stable and therefore way larger time steps can be taken than for an explicit scheme. The default implicit scheme in COMSOL is used, which is the implicit Euler method.

4.2 Grid Refinement Study

First a grid refinement study carried out in which the maximum temperature on the tungsten monoblock is evaluated as a function of number of mesh elements when the monoblock is subjected to a constant heat flux of 10 MW/m^2, as illustrated in Figure 23. The depicted red data points, indicate the simulated value of the maximum temperature of the tungsten monoblock as a function of the total number of mesh elements. While a clear grid independence is not reached yet when looking at the data points, the fitted trend suggests that the maximum temperature begins to asymptotically approach a converged value beyond approximately 1.2×10^6 elements. Ideally simulations with this amount of elements should be used for further analysis. However due to the significant computational costs of these simulations, and these meshes requiring over

four weeks of simulation time, this was not feasible within the time frame of this work. Therefore, the simulation results presented in the following sections are based on a mesh with 7.2×10^5 elements. Consequently, a slight underestimation of the temperature values is expected in the presented results in the following sections.

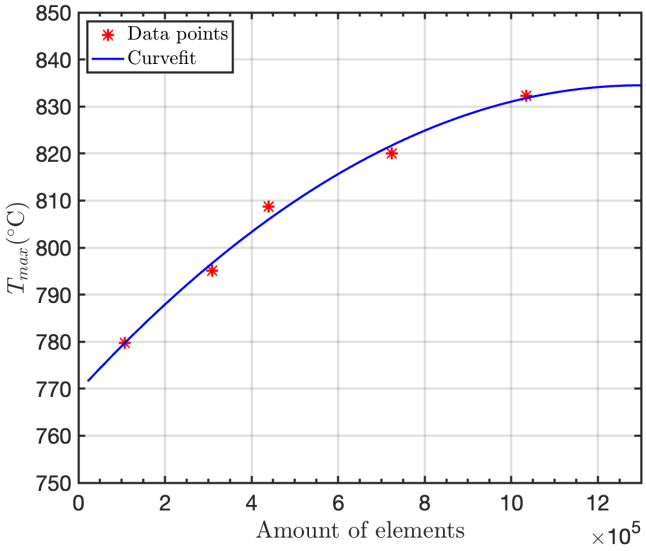

Figure 23: Simulated maximum temperature of the tungsten monoblock cooled by sCO_2 under an applied heat flux of 10 MW/m^2, plotted as a function of the total number of mesh elements used in the numerical domain.

4.3 Results & Discussion

In this section, the numerical results from two simulation cases are presented, wherein the tungsten monoblock is subjected to surface heat fluxes of 10 MW/m^2 and 20 MW/m^2. The analysis focuses on the temperature distribution within the tungsten monoblock, as well as the velocity and temperature fields of the sCO_2 flowing through the cooling tube.

4.3.1 Tungsten Block (Solid Domain)

The temperature profiles for both models are plotted and can be seen in Figure 24. The maximum temperature of the tungsten monoblock when cooled with sCO_2 and subjected to a surface heat flux of 10 MW/m^2 was found to be 820.08 °C. This is significantly lower than the temperature measured during experimental testing using water as the coolant [19], where a peak temperature of approximately 1100 °C was recorded with a two-color pyrometer. For the 20 MW/m^2 case the maximum found surface temperature was 1790.7°C, which is also considerably lower than the approximately 2000 °C which they measured when using water as the coolant. Even though the mesh was not refined enough and the maximum temperature will be higher, the margins are big enough to conclude that using sCO_2 results in a lower surface than water.

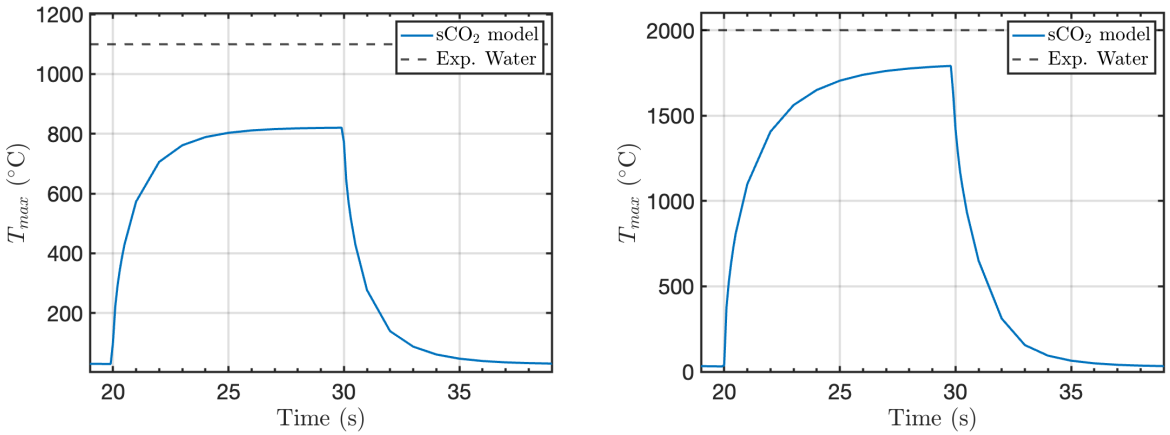

(a) Heat load is 10 MW/m^2

(b) Heat load is 20 MW/m^2

Figure 24: Comparison of the predicted maximum temperature of the tungsten monoblock using sCO_2 as the coolant with the experimentally measured maximum temperature using water as the coolant. Simulations and experiments are performed under identical heat flux conditions and equal pumping power for both fluids.

The temperature contour of the top surface of the monoblock for both cases can be seen in Figures 25 and 26. The results of all of the figures in this section are taken at 29.8 seconds because this is when the temperatures were the highest. It can be seen that the highest temperature occurs around the middle of the heated part at the corners for both cases, which is in line with previous research when water was used [19, 21]. The reason the maximum surface temperature occurs somewhere in the middle is that heat can conduct only in the negative y-direction, whereas at the edges it also conducts in the z-direction to the lower temperature non heated tungsten as shown in Figure 27 for the 20 MW/m^2 case. This effect might be over-predicted in comparison with the experimental data due to the gaps that are not modelled.

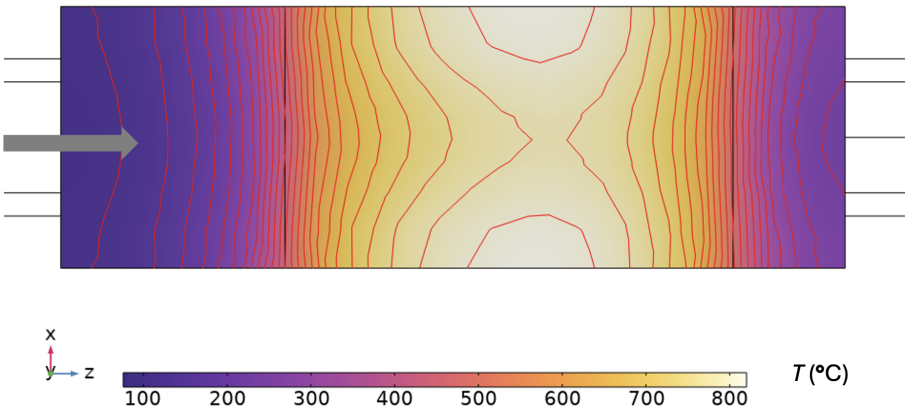

Figure 25: Predicted temperature profile on the top surface of the tungsten monoblock where a heat flux of 10 MW/m^2 is applied (t = 29.8 s). The region between the two vertical black lines is where the heat flux is applied.

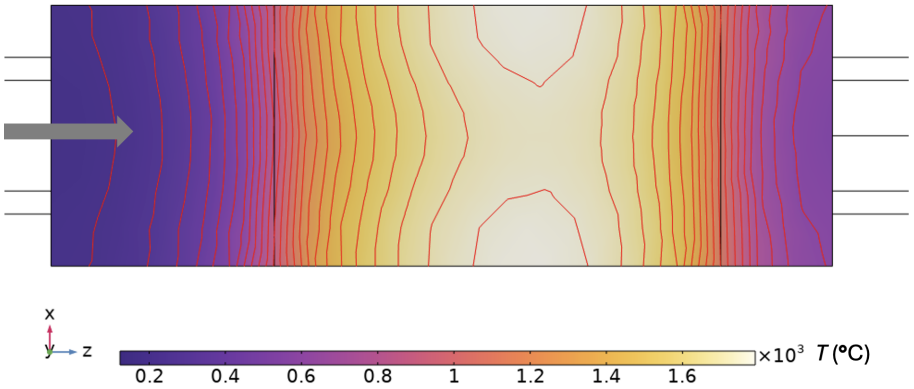

Figure 26: Predicted temperature profile on the top surface of the tungsten monoblock where a heat flux of 20 MW/m^2 is applied (t = 29.8 s). The region between the two vertical black lines is where the heat flux is applied.

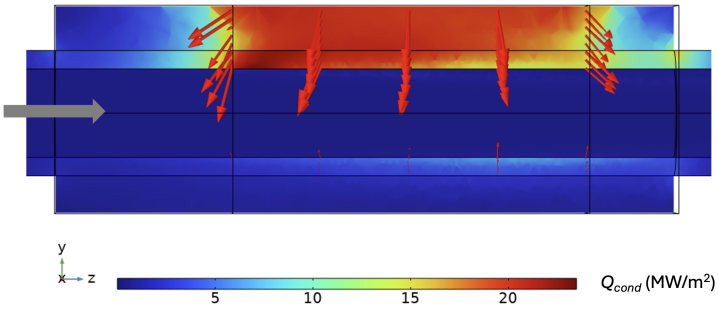

Figure 27: Side view of the tungsten monoblock illustrating the applied heat flux distribution on the top surface under a uniform heat load of 20 MW/m^2 (t = 29.8 s). The arrow sizes are scaled proportionally to represent the relative magnitude of the heat flux.

The cross-section temperature contours of the hottest region at $z = 173$ mm can be seen in Figure 28. Once again it can clearly be seen that the highest temperatures are reached in the corners for both cases, due to the corners being further away from the coolant. The recrystallization temperature of 1550°C for tungsten still gets reached for the high heat flux transients. It can also be seen that the melting temperature of copper of 1085 °C is not reached in the copper domain for both cases. For the interlayer the temperature gets really close to the melting temperature for the 20 MW/m^2 case, but since the interlayer has no structural function it is not a problem as long it does not reach the melting temperature. As mentioned before the temperatures are under-predicted, so if the copper appears to reach the melting temperature for a grid independent solution, the armor thickness needs to be increased from 6 mm for further research. This comes at the cost of increasing the maximum surface temperature at the plasma facing tungsten. The temperature in the CuCrZr piping will exceed the recrystallization temperature of approximately 430 °C for the top half of the tube, so after a lot of shut-down transients creep might occur in the piping as well. During steady operation the copper does not reach the recrystallization temperature so no degradation of the piping is expected. The actual internal thermal stresses and strains were not analyzed for this research but this same model and the found temperature fluctuations for the cycles could be used for such a study.

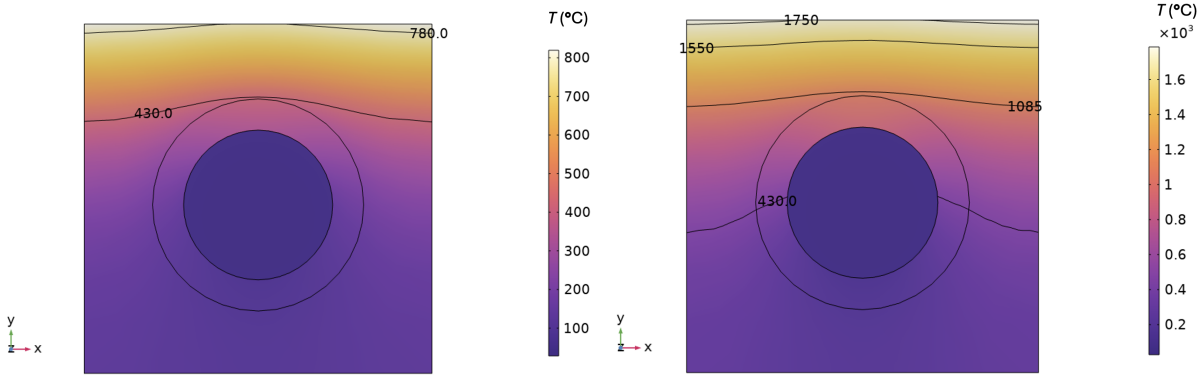

(a) Heat load is 10 MW/m^2

(b) Heat load is 20 MW/m^2

Figure 28: Cross sectional view of the tungsten monoblock, copper tubing, and cooling fluid indicating the predicted values of the temperature profile at the z=173 mm, the hottest location along z direction (t = 29.8 s).

4.3.2 Supercritical CO_2 (Fluid Domain)

To investigate the influence of buoyancy in the sCO_2 fluid on heat transfer, the buoyancy number Bu (see Equation 15), is plotted in Figure 29. It can be seen that the Bu number starts increasing as the fluid enters the section surrounded by the monoblock and decreases after it exits the monoblock. Also the Bu number is higher at the top due to the higher temperature (and thus bigger density difference with the bulk fluid) at the top since the monoblock is also heated from the top. The main differences between the two cases illustrated in Figure 29, is that the effect of buoyancy increases in an earlier section of the tube for 20 MW/m^2 case and that the buoyancy at the bottom remains lower for the 10 MW/m^2 case. This is expected because the sCO_2 will transition from the liquid-like to the gas-like fluid earlier near the walls due to the higher heat flux and the buoyancy is mainly dependent on the density differences within the flow. However, by looking at the magnitude of the buoyancy number it can be concluded that the influence of buoyancy compared to the inertia force is not very prominent for both cases since the Bu number remains below 0.001 [40]. The Reynolds, Grashof and Prandtl number for both cases can be found in Appendix D.

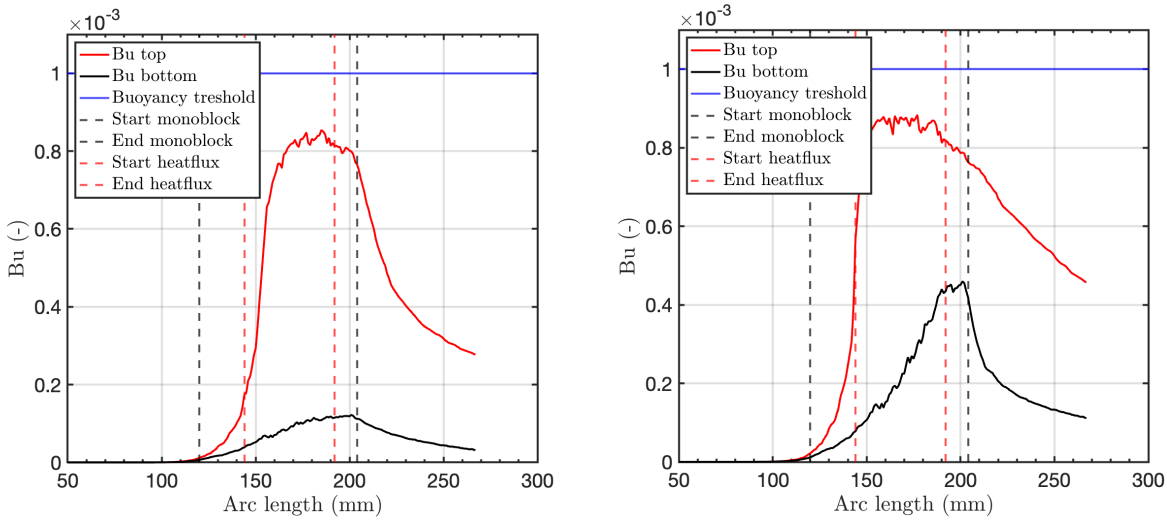

(a) 10 MW/m^2 applied

(b) 20 MW/m^2 applied

Figure 29: Buoyancy number evaluated for the sCO2 fluid domain (t = 29.8 s). The black and red dashed line on the left and right of the figures indicate the start and end of the tungsten monoblock and the heated section, respectively.

That the influence of buoyancy forces is not very high as compared to the inertia forces can also be concluded when looking at the streamlines for the 20 MW/m^2 case in Figure 30, where there can be seen that all of the streamlines are going almost straight. This is a big difference when comparing it with streamlines presented in Chapter 3. The reason for this is that the pointwise mass flux considered at the inlet of the tungsten monoblock is significantly higher than for geometry used for the feasibility study. This higher mass flux means a higher velocity (almost 10 times as high) and therefore a Reynolds number which is also approximately 10 times as high, resulting in low Bu number. The Grashof number is slightly higher for the monoblock than for the validation case, but since the Reynolds number is squared this influences the buoyancy more. Looking at the velocity profile in Figure 30, it can also be seen that the velocity near the top wall is higher than near the bottom wall downstream the heated length. This is in line with what was seen for the feasibility study carried out in Chapter 3. The reason for this increase in velocity is the lower density and the mass flux needing to be the same at the start and the end of the tube to satisfy the conservation of mass.

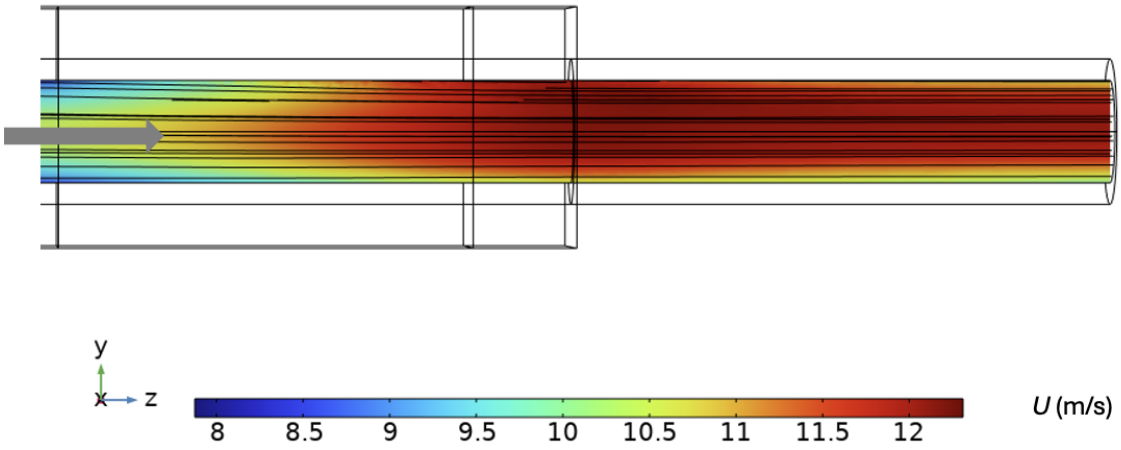

Figure 30: Side view velocity field and streamlines for the 20 MW/m^2 case, starting from the part where the heat flux is applied (z = 144 mm) (t = 29.8 s).

A longitudinal temperature profile in the sCO_2 fluid domain can be seen in Figures 31 and 32 for the case of 10 MW/m^2 and 20 MW/m^2 respectively. The color scale is chosen so that the fully liquid-like region (below 28 °C) is dark blue and the fully gas-like region (above 42 °C) is dark red, with the pseudocritical temperature of approximately 35 °C in the middle in white. When comparing the two cases, it can be seen that gas-like state is not fully reached for the 10 MW/m^2 case where the maximum temperature reached is 40.3 °C. For the 20 MW/m^2 case the maximum temperature was 57.3 °C, so the a fully gas-like state is reached. The gas-like region is reached at the top which is expected since the heat flux is also applied at the top. Due to the gas-like layer near the wall HTD is expected in this region. At the bottom side of the tube, the fluid also reaches the two-phase state which, which best visible for the 20 MW/m^2 case. At this bottom wall HTE is expected. For both cases it can be seen that the hot gas-like layer at the top increases in thickness along the length of the tube, but decreases in temperature due its mixing with the bulk flow. This mixing can be seen even more clearly in Figure 33, where the cross-section temperature just past the monoblock (z=208 mm) and at the end of the pipe (z=260 mm) are compared for the 20 MW/m^2 case. Just after the heated length there is a gas-like insulation layer almost all around the tube walls visible and further downstream this is mixed into a thicker, cooler two-phase layer. Also the bulk temperature is approximately two degrees higher here at approximately 30 °C.

It can be concluded that the previously approximated pumping power (see Section 2.3.1) needed per meter is an overestimation since a fully gas-like fluid was assumed after the heated length. Due to the assumption that the fluid would be fully gas-like, the velocity after the heated length has been greatly overestimated which is the biggest contributor to pumping power needed per meter. Taking this into account it can be concluded that using these inlet conditions would significantly reduce the energy required to pump the sCO2 fluid that what is currently used for water.

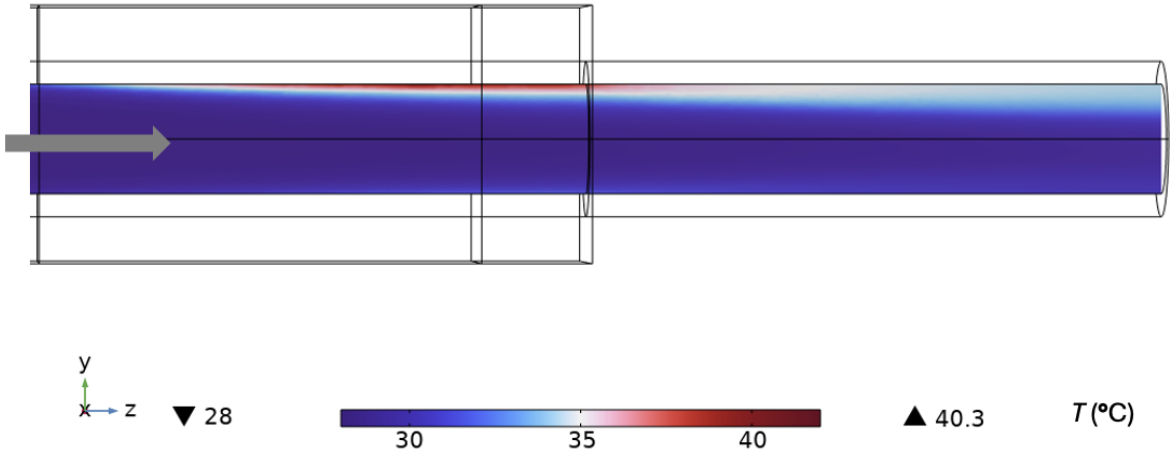

Figure 31: Side view temperature profile of the sCO_2 fluid starting from the heated region of the monoblock ($z = 144$mm) for the 10 MW/m^2 case ($t = 29.8$ s ; $p = 8.15$ MPa ; $T_{pc} \approx 35°C$).

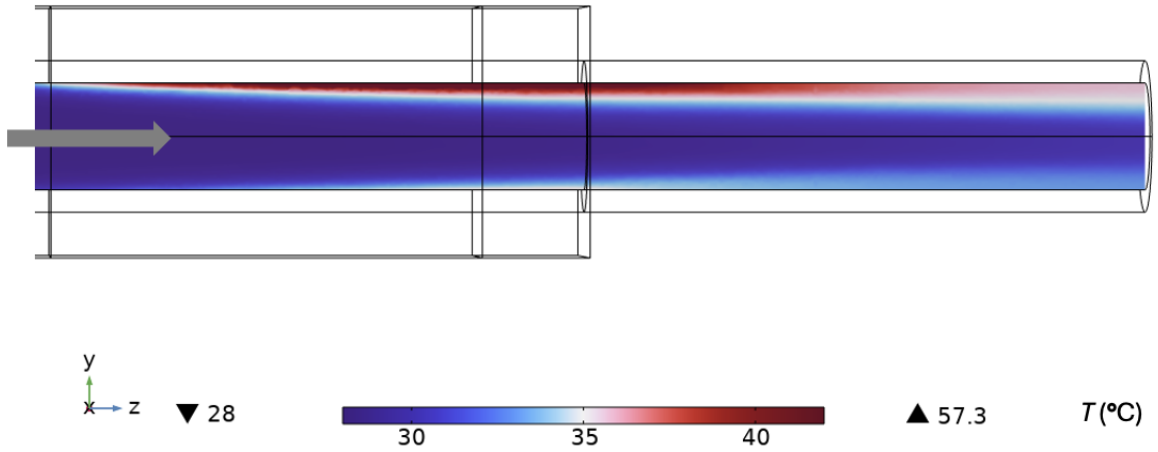

Figure 32: Side view temperature profile of the sCO_2 fluid starting from the heated region of the monoblock ($z = 144$mm) for the 20 MW/m^2 case ($t = 29.8$ s ; $p = 8.15$ MPa ; $T_{pc} \approx 35°C$).

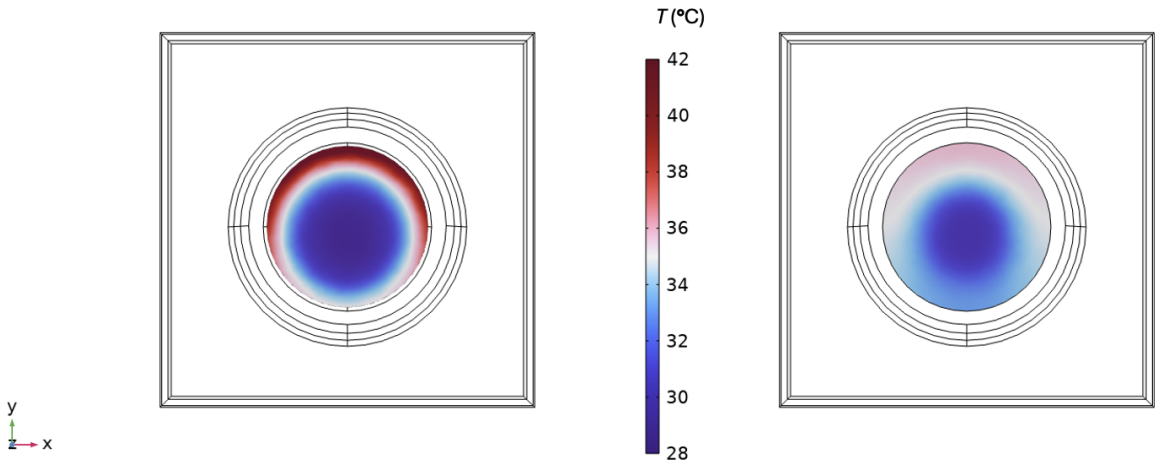

Figure 33: Cross-sectional temperature profile of the sCO_2 fluid just after the monoblock (z=208 mm) on the left and at the end of the pipe (z=260 mm) on the right for the 20 MW/m^2 case (t = 29.8 s ; p = 8.15 MPa ; $T_{pc} \approx 35°C$).

To see if HTE or HTD is happening the heat transfer coefficient (HTC) is determined using the Dittus-Boelter relation presented in Chapter 2 (see Equation 8) and with the general heat transfer coefficient equation (see Equation 10). They are divided by each other and are plotted over the heated length (which is schematically displayed in Figure 34) for both cases in Figure 35.

For the 10 MW/m^2 case it can be seen that the HTC at the bottom remains fairly constant, but at the top it first raises and then decreases along the heated length of the tube. The reason for this peak is that the fluid temperature near the wall approaches the pseudocritical temperature of approximately 35 °C and pseudo-boiling happens at that location. Once passed this point the HTC decreases again. This is in line with what was found with experimental testing of supercritical fluids from the literature as given in Section 2.5. The ratio of the HTCs then remains above 1 for the remainder of the heated length, which was expected since the fully gas-like state is not reached, so a gas-like insulation layer causing HTD will not appear.

For the 20 MW/m^2 case the HTC already starts high at the top due to the massive heat flux the fluid almost instantly reaches the pseudo critical temperature. Further downstream the HTC drops rapidly because of the fluid becoming fully gas like, and at around half of the heated length at z = 170 the ratio of HTCs becomes lower than 1, which means that HTD occurs here. The temperature near the wall fully reaches the gas-like state and an insulation layer appears. At the bottom wall the opposite happens. The HTC starts already fairly high and then gradually increases further downstream. This is once again due to the fluid reaching the two-phase temperature, approaching the Widom-line, which was also clearly visible in Figure 32. This increase at the bottom is more gradually than it was at the top for the 10 MW/m^2 case because the heat flux at the bottom wall is considerably lower.

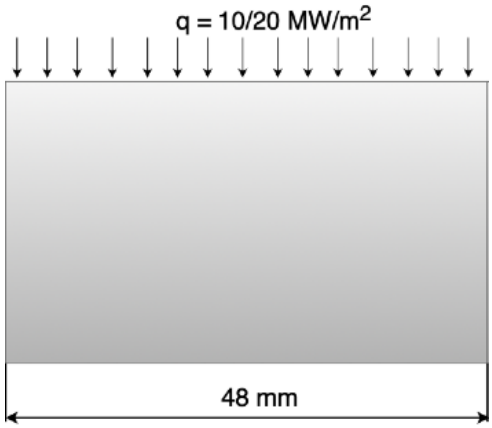

Figure 34: The region where the heat transfer coefficient (HTC) is analyzed.

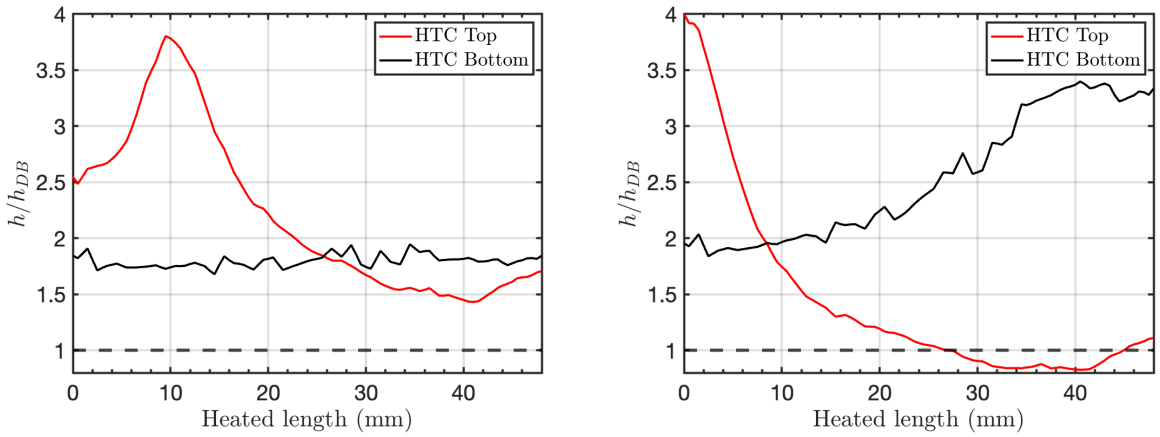

(a) Heat load is 10 MW/m^2

(b) Heat load is 20 MW/m^2

Figure 35: Ratio of the heat transfer coefficients determined by Dittus-Boelter (Equation 8) and the general equation (Equation 10) (t = 29.8 s).

4.4 Concluding Remarks

Overall, from the above results it can been concluded that HTD does not occur for the tungsten monoblock design under a steady-state heat load of 10 MW/m^2, but it does occur for the 20 MW/m^2 shut-down transient. This is as expected when looking at the HTD onset curve in Figure 36. It can be seen that the steady state case is at the line and that shut-down transient case significantly exceeds it. In order to combat this there can be chosen to increase the mass flux to 10000 kg/m^{2}s so the shut down transient also goes below this line.

The pumping power needed per meter was previously overestimated since a fully gas-like fluid of above 42 °C was assumed after the heated length which overestimates the velocity, which is the biggest contribution to the pumping power needed (see Equation 6). Knowing that most of the fluid is in the two-phase state past the heated length, a better approximation is made for the pumping power needed per meter. The properties for the two-phase state are approximated as the average between the liquid-like and gas-like state properties in Table 1. With these new

findings, and using the method described in Section 2.3.1, a mass flux of 9300 kg/m^{2}s is calculated which would result in the same energy costs as water (116 W per meter). The resulting needed power before and after the heated length are calculated and displayed in Table 4. Using this calculated higher mass flux at the inlet might reduce the temperatures found in the monoblock, but a reduction in HTE can also occur when increasing the mass flux by too much as mentioned in Section 2.6.

Table 4: Energy loss when assuming fully two-phase flow past heated length.

Property	sCO_2 liquid-like	sCO_2 two-phase-like
Pointwise mass flux G	9300 kg/m^{2}s	9300 kg/m^{2}s
Pressure	8.15 MPa	8.15 MPa
Viscosity μ	$6.16 * 10^{-5}$ kg/ms	$4.195 * 10^{-5}$ kg/ms
Density ρ	742 kg/m^3	508 kg/m^3
Axial velocity v	12.5 m/s	18.3 m/s
P_{pump} per meter	79.1 W	153.2 W

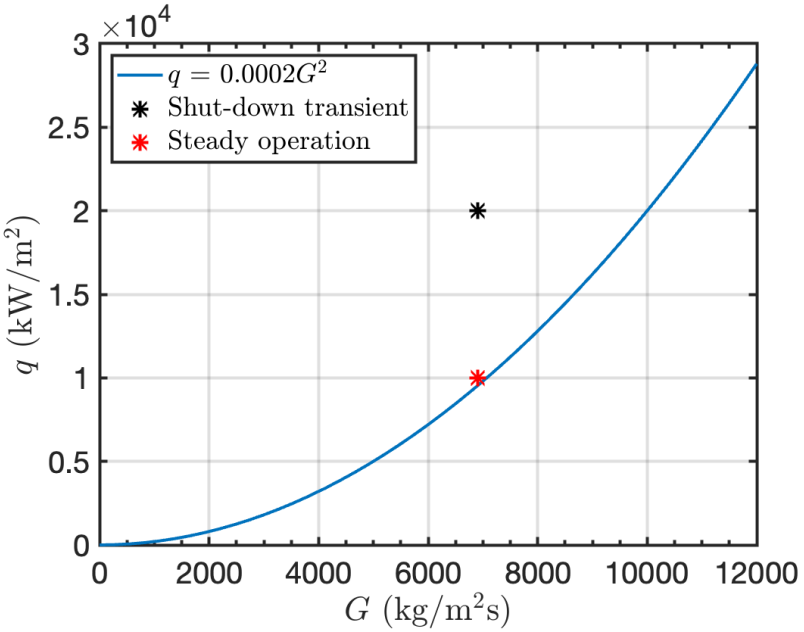

Figure 36: Criteria for the onset of Heat Transfer Deterioration (HTD) as suggested from Kim et al. [7] (solid blue curve). The markers represent the two cases simulated in this chapter for tungsten monoblock.

5 Conclusion

This thesis investigates the cooling behavior of sCO_2 under extreme heat fluxes, with a particular focus on cooling the divertor of future nuclear fusion reactors. The study focuses on a conjugate heat transfer problem involving a tube geometry through which sCO_2 flows while being subjected to an external heat flux. First the thermophysical properties were analyzed to determine the optimal operating range to use sCO_2 as a coolant. It was found that when sCO_2 transitions from a liquid-like to a gas-like state and crosses the so-called Widom-line, pseudo-boiling happens which results in superior heat transfer performance over conventional coolants like water.

To determine the feasibility of modeling this pseudo-boiling phenomenon, a numerical study was conducted using COMSOL. This study evaluated whether the highly non-linear variations in thermophysical properties of sCO_2 could be captured. Simulations were carried out for moderate heat fluxes, and the results were compared with available experimental and numerical data from literature. Due to the limited computational resources and time, the k-ϵ turbulence model was employed instead of the SST turbulence model which is used more frequently for similar numerical studies. Despite using this less accurate turbulence and a relatively coarser mesh than previous studies, the simulations qualitatively captured key characteristics of supercritical heat transfer, including the heat transfer enhancement (HTE) and heat transfer deterioration (HTD). However, quantitative differences in the wall temperatures were observed between the numerical model and the experimental results in the literature. Near the entrance region of the heated section, the temperatures were under-predicted and further downstream the temperature were over-predicted. The deviations were primarily caused by insufficient mesh resolution, which reduced the accuracy of local temperature gradients and thermophysical properties which influences the flow patterns. Nevertheless, the overall found trends in wall temperatures, as well as the variations of temperature, velocity, and density within the fluid domain, were in reasonable qualitative agreement with reference data from the literature.

Based on this feasibility study, the research was extended to the cooling of tungsten monoblocks in the ITER divertor, which are subjected to heat fluxes of 10 MW/m^2 and 20 MW/m^2. The same numerical approach was performed to evaluate the performance of sCO_2 as a coolant in this extreme environment for the new geometry. Using an equivalent pumping power, the numerical model using sCO_2 showed a lower peak temperature in the tungsten monoblock than the literature which used water. From the results of the feasibility study it was concluded that this temperature is an under-estimate of the actual temperature, but the difference in values is sufficiently large to conclude that sCO_2 outperforms water. This improvement is attributed to the high heat transfer coefficients which are caused by the pseudo-boiling in the flow channel beneath the heated monoblock. Further analysis using the buoyancy number showed that the overall buoyancy effects were negligible for the used mass flux. This minimizes the risk of heat transfer deterioration caused by low density gas rising to the upper walls of the flow channel.

In summary, the results of this study demonstrate that sCO_2 is a promising candidate for thermal management in high heat flux applications. Its superior heat transfer characteristics under pseudo-boiling conditions, along with its better compatibility with liquid metals, makes it a suitable coolant in future liquid metal divertor technology.

6 Recommendations

6.1 Memory Problems Feasibility Study

As mentioned before, the analyzed results were not fully grid independent yet. For the validation case it was impossible to refine further due to memory issues. Using two nodes at once on the cluster should double the amount of available memory, but during initial tries the out-of-memory error still occurred during the beginning of the simulation and only the memory of 1 node seemed to be used. It will be very beneficial for further simulations using COMSOL to try to get this working properly. Finer meshes are possible in that case, and even using the more accurate SST turbulence might be possible if y^+ can be kept below 1.

Another method that was tried to combat the memory problems for the validation case is trying to divide the model into parts, and using the outlet conditions of the previous section as the inlet conditions for the next section. Implementing this proved to be challenging, and due to time constraints associated with this thesis, further attempts were discontinued. However, if this challenge can be addressed in future work, it may enable the use of finer meshes and therefore improve the accuracy of the simulations.

6.2 Monoblock Model

Unfortunately a fully grid independent solution was not achieved for the simulations of the tungsten monoblock due to the amount of available time. However, the observed trend from the mesh refinement study, as illustrated in Figure 23 using a fitted curve, indicates that grid independence was almost achieved. At the time of writing this thesis, two additional simulations for both the 10 MW/m^2 and 20 MW/m^2 cases have been submitted to the cluster with approximately 1.6 million elements. The results from these simulations can be incorporated into Figure 23 in future work to see if grid independence is reached. If this is the case, the results of these simulations can be used for an improved approximation of the temperatures found within the tungsten monoblock.

From a previous numerical research using water as a coolant in a monoblock model, it was found that adding a metallic swirl-tape inside the tube carrying the coolant increases the heat transfer and lowers the temperatures in the tungsten [20]. From another previous experimental set-up with sCO_2, it was found that adding latices inside the coolant tube, stops the gas-like layer from forming near the wall which also increased the heat transfer [51]. An interesting research can be done by implementing both a swirl tape and lattices in this monoblock model to see which of these options increases the heat transfer the most.

6.3 Liquid Metal Divertor

From a previous numerical research using high pressure water, promising results were found for the Liquid Metal Divertor design. A schematic overview can be seen in Figure 37. On the top part the heat flux is applied and the liquid tin flows between the 3D-printed tungsten Capillary Porous System (CPS). The parameter t, which is the thickness of the CPS, can be chosen ranging from 1 mm up until 3 mm. They found that the using CuCrZr as the coolant housing could

withstand the highest heat loads. The temperature and pressure of the coolant were carefully chosen so that the tin remains above the melting temperature of 243°C, which is why the chosen inlet temperature of the coolant is so high at 180°C [8].

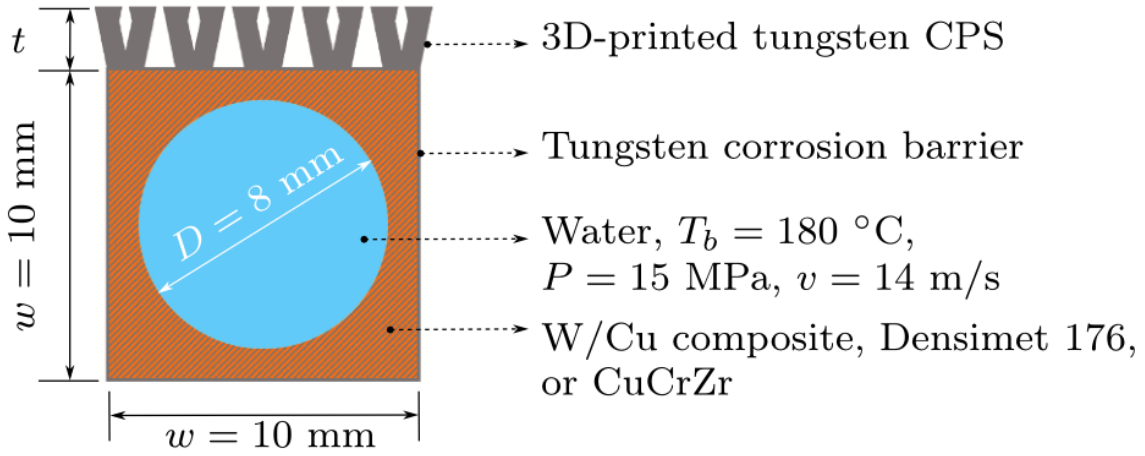

Figure 37: A cross-sectional schematic representing the liquid metal divertor technology where a liquid metal (typically tin), flows through the tungsten CPS which faces the plasma. This tin is in turn cooled by the coolant flowing underneath inside the tube. [8]

Since sCO_2 operates at a significantly lower temperature, a crude 1D heat transfer analysis is done to determine if the tin remains liquid when using sCO_2 at 28°C as a coolant. The thermal resistance in series is calculated as follows:

$$R_{total} = R_{tin} + R_{CuCrZr} + R_{sCO_2} = \frac{t}{k_{tin}} + \frac{0.001}{k_{CuCrZr}} + \frac{1}{h_{sCO_2}} \tag{33}$$

where k is the thermal conductivity of the materials and h is the heat transfer coefficient of the sCO_2. This heat transfer coefficient fluctuates a lot as seen before, so the highest found value for the previous monoblock testing of approximately 75 kW/m^{2}K is used. The thermal conductivity of liquid tin was found to be approximately 30 W/mK and for CuCrZr 330 W/mk. Filling this in resulted in a thermal resistance of $4.97 \cdot 10^{-5}$ K/W for $t = 0.001$ m and $1.164 \cdot 10^{-4}$ K/W for $t = 0.003$ m. The temperature difference between the surface of the channel and the plasma facing tin can then be calculated as follows:

$$R_{total} = \frac{\Delta T}{q}, \implies \Delta T = R_{total} * q \tag{34}$$

which results in a temperature difference for steady state operation of 497 °C for $t = 0.001$ m and 1163 °C for $t = 0.003$ m. Since the temperature at the CuCrZr wall is 28 °C minimum (coolant inlet temperature), it can be concluded that it is possible to at least have liquid tin at the plasma facing surface which is the most important requirement. The lowest possible temperature at the tin and CuCrZr interface can be calculated as follows:

$$T_{interface} = \frac{R_{CuCrZr}}{R_{CuCrZr} + R_{tin}} \Delta T + 28 \tag{35}$$

which results in a temperature of approximately 42.6 °C for $t = 0.001$ m and 58.3 °C for $t = 0.003$ m. This means that when keeping this exact design, there will also be solid tin near the cooling channels. The thickness of this solid tin will fluctuate, depending primarily on the heat transfer coefficient in the sCO_2 flow.

Since the plasma facing surface tin is still liquid during steady state operation, this design could still work with sCO_2 and it is still interesting for further numerical research. It is advised to use the maximum tin thickness of 3 mm for the initial models and see how much of the tin becomes solid and if this gives complications with the tin flow.

References

[1] J. Cizek, M. Vilémová, F. Lukac, M. Koller, J. Kondas, and R. Singh, "Cold sprayed tungsten armor for tokamak first wall," *Coatings*, vol. 9, p. 836, 12 2019.

[2] ITER Organization, "first-sector-unveiled," 2020. `https://www.iter.org/node/20687/first-sector-unveiled`.

[3] W. Dekeyser, D. Reiter, and M. Baelmans, "Divertor target shape optimization in realistic edge plasma geometry," *Nuclear Fusion*, vol. 54, p. 073022, 05 2014.

[4] R. Pitts, S. Bardin, B. Bazylev, M. van den Berg, P. Bunting, S. Carpentier-Chouchana, J. Coenen, Y. Corre, R. Dejarnac, F. Escourbiac, J. Gaspar, J. Gunn, T. Hirai, S.-H. Hong, J. Horacek, D. Iglesias, M. Komm, K. Krieger, C. Lasnier, G. Matthews, T. Morgan, S. Panayotis, S. Pestchanyi, A. Podolnik, R. Nygren, D. Rudakov, G. De Temmerman, P. Vondracek, and J. Watkins, "Physics conclusions in support of iter w divertor monoblock shaping," *Nuclear Materials and Energy*, vol. 12, pp. 60–74, 2017. Proceedings of the 22nd International Conference on Plasma Surface Interactions 2016, 22nd PSI.

[5] L. Cheng, J. Xu, W. Cao, K. Zhou, and G. Liu, "Supercritical carbon dioxide heat transfer in horizontal tube based on the froude number analysis," *Energy*, vol. 294, p. 130980, 2024.

[6] X. Xie, D. Ye, J. Gong, S. Zhao, and J. Wang, "Influence of conjugate thermal boundary on turbulent heat transfer of supercritical co2 in the horizontal tube," *Applied Thermal Engineering*, vol. 248, p. 123182, 2024.

[7] J. Kim, H. Jeon, J. Yoo, and J. Lee, "Experimental study on heat transfer characteristics of turbulent supercritical flow in vertical circular/non-circular tubes," in *Proceedings of the 11th International Topical Meeting on Nuclear Reactor Thermal-Hydraulics (NURETH-11)*, (Avignon, France), Oct. 2005. October 2–6.

[8] P. Rindt, J. van den Eijnden, T. Morgan, and N. Lopes Cardozo, "Conceptual design of a liquid-metal divertor for the european demo," *Fusion Engineering and Design*, vol. 173, p. 112812, 2021.

[9] ITER Organization, "External heating systems," 2017. `https://www.iter.org/machine/supporting-systems/external-heating-systems`.

[10] ITER Organization, "Magnets - ITER," 2025. `https://www.iter.org/machine/magnets`.

[11] J. J. Chapman, "Advanced fusion reactors for space propulsion and power systems," Technical Publication NASA/TP-2009-214784, NASA Langley Research Center, 2009. NASA Technical Report Server (NTRS).

[12] L. L. N. Laboratory, "Achieving fusion ignition," 2023. `https://lasers.llnl.gov/science/achieving-fusion-ignition`.

[13] EUROfusion, "History of fusion," 2023. `https://euro-fusion.org/fusion/history-of-fusion/`.

[14] ITER Organization, "The tao of q," 2017. https://www.iter.org/node/20687/tao-q.

[15] FutureLearn, "Frontier physics, future technologies," 2023. https://www.futurelearn.com/info/courses/frontier-physics-future-technologies/0/steps/228802.

[16] ITER Organization, "What will iter do?." https://www.iter.org/fusion-energy/what-will-iter-do.

[17] ITER Organization, "Turning neutrons into electricity," 2023. https://www.iter.org/node/20687/turning-neutrons-electricity.

[18] ITER Organization, "Cooling water," 2023. https://www.iter.org/machine/supporting-systems/cooling-water.

[19] T. Hirai, S. Panayotis, V. Barabash, C. Amzallag, F. Escourbiac, A. Durocher, M. Merola, J. Linke, T. Loewenhoff, G. Pintsuk, M. Wirtz, and I. Uytdenhouwen, "Use of tungsten material for the iter divertor," *Nuclear Materials and Energy*, vol. 9, pp. 616–622, 2016.

[20] S. E.-D. El-Morshedy, "Thermal-hydraulic simulation of iter tungsten divertor monoblock for loss of flow transient," *Nuclear Materials and Energy*, vol. 38, p. 101616, 2024.

[21] J. You, E. Visca, T. Barrett, B. Böswirth, F. Crescenzi, F. Domptail, G. Dose, M. Fursdon, F. Gallay, H. Greuner, K. Hunger, A. Lukenskas, A. Müller, M. Richou, S. Roccella, C. Vorpahl, and K. Zhang, "High-heat-flux technologies for the european demo divertor targets: State-of-the-art and a review of the latest testing campaign," *Journal of Nuclear Materials*, vol. 544, p. 152670, 2021.

[22] ITER Organization, "Making it work," 2023. https://www.iter.org/fusion-energy/making-it-work.

[23] Energy Encyclopedia, "Divertor - Tokamaks," 2025. https://www.energyencyclopedia.com/en/nuclear-fusion/tokamaks/divertor.

[24] COMSOL AB, *COMSOL Multiphysics® v6.0*. COMSOL AB, Stockholm, Sweden.

[25] D. Banuti, M. Raju, P. Ma, M. Ihme, and J.-P. Hickey, "Seven questions about supercritical fluids - towards a new fluid state diagram," 01 2017.

[26] D. Banuti, "Crossing the widom-line – supercritical pseudo-boiling," *The Journal of Supercritical Fluids*, vol. 98, 01 2015.

[27] P. Linstrom and W. Mallard, "Nist chemistry webbook, nist standard reference database number 69." http://webbook.nist.gov, 2025. Chapter from NIST Chemistry WebBook.

[28] R. Span and W. Wagner, "A new equation of state for carbon dioxide covering the fluid region from the triple-point temperature to 1100 k at pressures up to 800 mpa," *Journal of Physical and Chemical Reference Data*, vol. 25, pp. 1509–1596, 11 1996.

[29] M. L. Huber, E. A. Sykioti, M. J. Assael, and R. A. Perkins, "Reference correlation of the thermal conductivity of carbon dioxide from the triple point to 1100 k and up to 200 mpa," *Journal of Physical and Chemical Reference Data*, vol. 45, p. 013102, 02 2016.

[30] A. Laesecke and C. D. Muzny, "Reference correlation for the viscosity of carbon dioxide," *Journal of Physical and Chemical Reference Data*, vol. 46, p. 013107, 03 2017.

[31] J. Luettmer-Strathmann, J. V. Sengers, and G. A. Olchowy, "Non-asymptotic critical behavior of the transport properties of fluids," *The Journal of Chemical Physics*, vol. 103, pp. 7482–7501, 11 1995.

[32] V. Vesovic, W. A. Wakeham, G. A. Olchowy, J. V. Sengers, J. T. R. Watson, and J. Millat, "The transport properties of carbon dioxide," *Journal of Physical and Chemical Reference Data*, vol. 19, pp. 763–808, 05 1990.

[33] A. Fenghour, W. A. Wakeham, and V. Vesovic, "The viscosity of carbon dioxide," *Journal of Physical and Chemical Reference Data*, vol. 27, pp. 31–44, 01 1998.

[34] G. Pintsuk, I. Bobin-Vastra, S. Constans, P. Gavila, M. Rödig, and B. Riccardi, "Qualification and post-mortem characterization of tungsten mock-ups exposed to cyclic high heat flux loading," *Fusion Engineering and Design*, vol. 88, no. 9, pp. 1858–1861, 2013. Proceedings of the 27th Symposium On Fusion Technology (SOFT-27); Liège, Belgium, September 24-28, 2012.

[35] M. Holmgren, "X steam, thermodynamic properties of water and steam," 2025. MATLAB Central File Exchange, Retrieved March 26, 2025.

[36] P. I. P. Leijendeckers, *Polytechnisch Zakboekje*. Den Haag, The Netherlands: Koninklijke PBNA, 48e druk ed., 1997.

[37] B. Zhu, J. Xu, X. Wu, J. Xie, and M. Li, "Supercritical "boiling" number, a new parameter to distinguish two regimes of carbon dioxide heat transfer in tubes," *International Journal of Thermal Sciences*, vol. 136, pp. 254–266, 2019.

[38] D. Banuti, "The latent heat of supercritical fluids," *Periodica Polytechnica Chemical Engineering*, vol. 63, pp. 270–275, Jan. 2019.

[39] X. Xu, L. Teng, W. Ran, Y. Wang, and C. Liu, "A review of heat transfer deterioration mechanisms and mitigation strategies of supercritical co2 heat transfer," *International Journal of Heat and Fluid Flow*, vol. 109, p. 109534, 2024.

[40] K. Theologou, R. Mertz, E. Laurien, and J. Starflinger, "Experimental investigations on heat transfer of co2 under supercritical pressure in heated horizontal pipes," *Energy*, vol. 254, p. 124171, 2022.

[41] L. Cheng, Q. Wang, and J. Xu, "Supercritical heat transfer of co2 in horizontal tube emphasizing pseudo-boiling and stratification effects," *International Journal of Heat and Mass Transfer*, vol. 220, p. 124953, 2024.

[42] T. Wan, M. Zhou, P. Zhao, *et al.*, "Challenges in the modeling and simulation of turbulent supercritical fluid flows and heat transfer," *Propulsion and Energy*, vol. 1, p. 6, 2025.

[43] Z. Yang, H. Wang, B. Guan, H. Yang, Z. Li, and G. Wang, "Experimental and numerical investigation on the mechanisms of novel heat transfer deterioration of supercritical co2 in vertical tubes," *International Communications in Heat and Mass Transfer*, vol. 153, p. 107384, 2024.

[44] F. Buzzi, A. Pucciarelli, and W. Ambrosini, "On the mechanism of final heat transfer restoration at the transition to gas-like fluid at supercritical pressure: A description by cfd analyses," *Nuclear Engineering and Design*, vol. 355, p. 110345, 2019.

[45] M. Nabil and A. S. Rattner, "Large eddy simulations of high-heat-flux supercritical co2 convection in microchannels: Mixed convection and non-uniform heating," *International Journal of Heat and Mass Transfer*, vol. 145, p. 118710, 2019.

[46] COMSOL, "Modeling subsurface co2 storage with comsol multiphysics," 2025. `https://www.comsol.com/video/modeling-subsurface-co2-storage-with-comsol-multiphysics`.

[47] COMSOL, "Comsol multiphysics documentation: Fluid flow interface," 2025. `https://doc.comsol.com/6.1/doc/com.comsol.help.cfd/cfd_ug_fluidflow_single.06.088.html`.

[48] C. Rumsey, "Implementing turbulence models into the compressible rans equations," 2014. `https://turbmodels.larc.nasa.gov/implementrans.html`.

[49] A. Bakker, "Lectures on applied computational fluid dynamics." Online, 2008. `https://www.bakker.org/Lectures-Applied-CFD.pdf`.

[50] R. Tian, X. Dai, D. Wang, *et al.*, "Study of variable turbulent prandtl number model for heat transfer to supercritical fluids in vertical tubes," *Journal of Thermal Science*, vol. 27, pp. 213–222, 2018.

[51] X. Wang, Y. Wang, X. Xiao, Z. Chen, Y. Kang, and Y. Lei, "Numerical study on heat transfer deterioration of supercritical co2 in lattice structure array channel," *International Journal of Heat and Mass Transfer*, vol. 227, p. 125600, 2024.

[52] S. hui Liu, Y. ping Huang, J. feng Wang, and L. K. Leung, "Numerical investigation of buoyancy effect on heat transfer to carbon dioxide flow in a tube at supercritical pressures," *International Journal of Heat and Mass Transfer*, vol. 117, pp. 595–606, 2018.

[53] COMSOL, "Comsol multiphysics documentation: Fluid flow interface," 2025. `https://doc.comsol.com/5.5/doc/com.comsol.help.cfd/cfd_ug_fluidflow_single.06.091.html`.

[54] FluidMechanics101, "[CFD] Inflation Layers / Prism Layers in CFD," 2021. `https://www.youtube.com/watch?v=1gSHN99I7L4&t=2687s`.

[55] FluidMechanics101, "What are wall functions and how do they work?," 2019. `https://www.youtube.com/watch?v=fJDYtEGMgzs&list=LL&index=1`.

[56] CFDOnline, "Standard k-epsilon model," 2025. https://www.cfd-online.com/Wiki/Standard_k-epsilon_model.

[57] COMSOL, *The k-ε Turbulence Model*, COMSOL 5.5. https://doc.comsol.com/5.5/doc/com.comsol.help.cfd/cfd_ug_fluidflow_single.06.088.html.

[58] Langley Research Center, "Turbulence modeling resource: The chien k-epsilon turbulence model," 2015. https://turbmodels.larc.nasa.gov/ke-chien.html.

[59] COMSOL, "Understanding the fully coupled vs. segregated approach and direct vs. iterative linear solvers," n.d. https://www.comsol.com/support/knowledgebase/1258.

[60] FluidMechanics101, "[cfd] meshing guide for pipes and ducts (o-grid, hexcore, polyhedra)." YouTube video, 2023. https://www.youtube.com/watch?v=32cRwxAh2ys.

A Grid Refinement Study Feasibility Geometry

To determine the accuracy of the found results, a grid refinement study is done for the feasibility study. This is done by running the 198 kW/m^2 test case for a few different meshes with an increasing amount of elements and compare the results. To see if the buoyancy effect gets captured well, there is chosen to use the maximum temperature difference between the top and bottom outer surface for this.

For relatively coarse meshes of around 1.5-2 million elements the top and bottom surface temperatures profiles were still almost exactly the same, so the buoyancy effects were not captured at all. The simulations that did show a deviation are plotted in Figure A.1. It can be seen that the results still linearly increase up until the simulation with the finest mesh. This indicates that the mesh is not refined enough for fully accurate results. Unfortunately this was the finest mesh which could be achieved without running into memory and time problems, therefore this mesh is still chosen for the feasibility study.

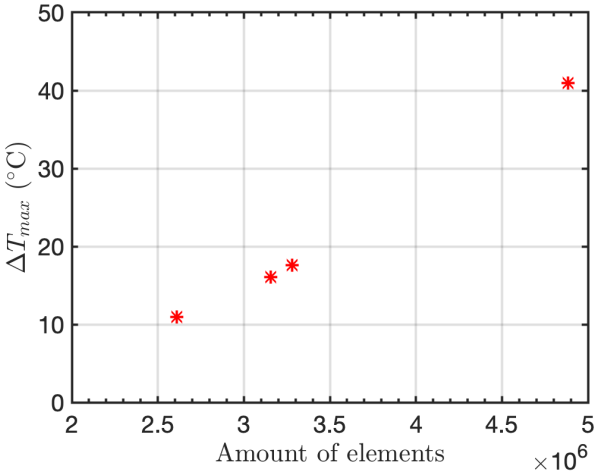

Figure A.1: Amount of elements versus the maximum temperature difference between the top and bottom wall

In order to get an idea of what further mesh refinement would have done, the mesh with approximately 3.3 million elements is compared with the finest possible mesh of approximately 4.9 million elements. The outer wall and bulk temperatures are compared with each other in Figure A.2. The following conclusions were drawn:

- The location where ΔT_{max} is achieved shifts slightly further downstream, so the bulk temperature reaches T_{pc} further downstream when refining the mesh
- The top wall temperature increases at the start of the heated length when refining the mesh, the bottom wall temperature remains the same for the first part
- For the second part of the heated length, the outer wall temperatures increase and the bulk temperature decreases when refining the mesh

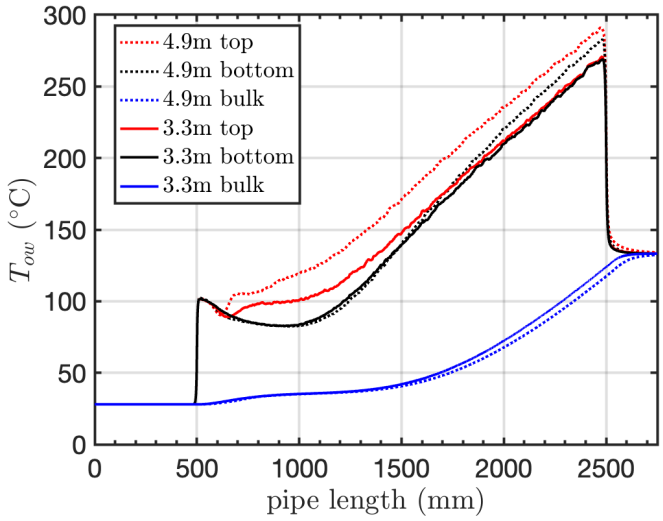

Figure A.2: Comparison between outer wall temperatures for 3.3 and 4.9 million elements.

B Changing Empirical Parameters $k-\epsilon$ Equations

Since the model results for the second part of the heated length gave an under-prediction of the heat transfer in comparison with the experimental data, there was chosen to change some of the parameters of the k-epsilon model and of the wall functions to try to better fit the experimental data. These parameters are empirically derived from experimental studies mostly employing subcritical fluids, so changing them to match the experimental data for this research might have been a solution.

The parameters that were changed and the reason why they were changed this way can be found in Table 5. The overall conclusion is that changing these parameters did not do much to the outer wall temperature profile, however the temperature at the end of the heated length did decrease for most of them. The temperature profiles from these tests, compared with the default model and the experimental data can be found below. The most promising result came from changing both $C_{1\epsilon}$ and $C_{2\epsilon}$ but since changing these parameters did not give the desired result, there is chosen to keep all the parameters as the default values for the rest of the research.

Table 5: Parameters that were changed

Parameter	New value	Reason
μ_T	$0.85 > 0.62$	Lowering turbulent Prandtl number gave better results for previous research with super critical fluids [50, 42]
B	$5.2 > 0$	Decreasing the B for the wall function decreases the velocity near the wall which should increases turbulence generated near wall, which should increase heat transfer
$C_{1\epsilon}$	$1.44 > 2$	Increases the turbulence production term
$C_{2\epsilon}$	$1.9 > 1$	Decreases the turbulence destruction term
$C_{1\epsilon}$ and $C_{2\epsilon}$	$1.44 > 2$ and $1.9 > 1$	Changing both production and destruction of turbulence

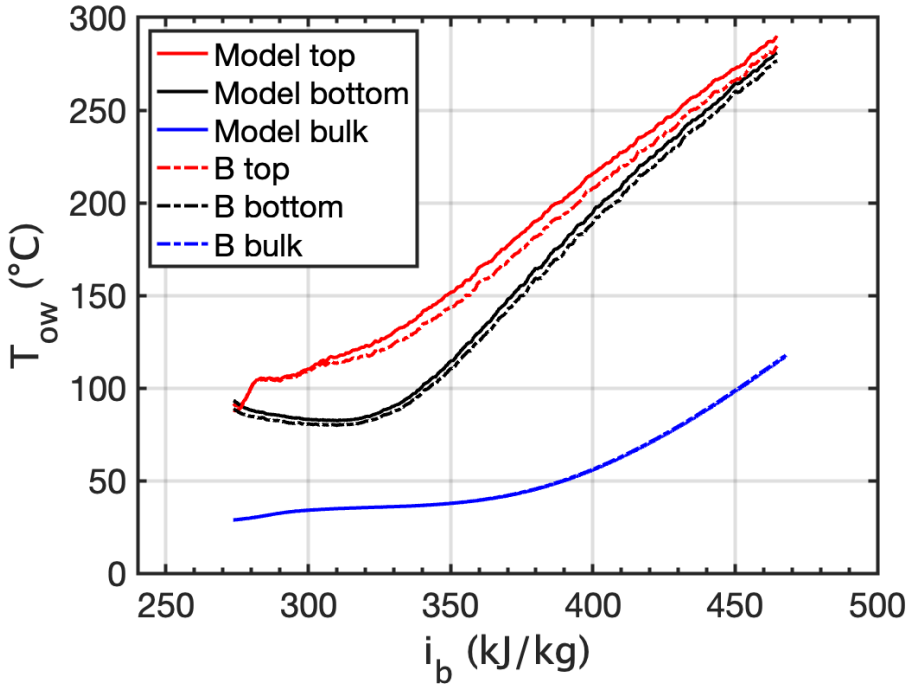

Figure B.1: Temperature profile for changing the value of B

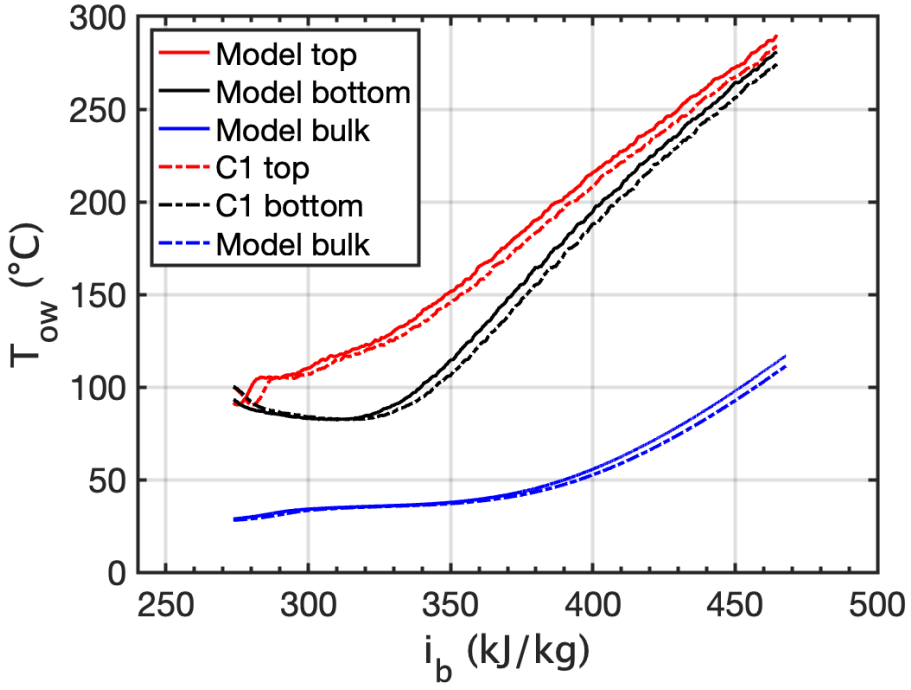

Figure B.2: Temperature profile for changing the value of $C_{1\epsilon}$

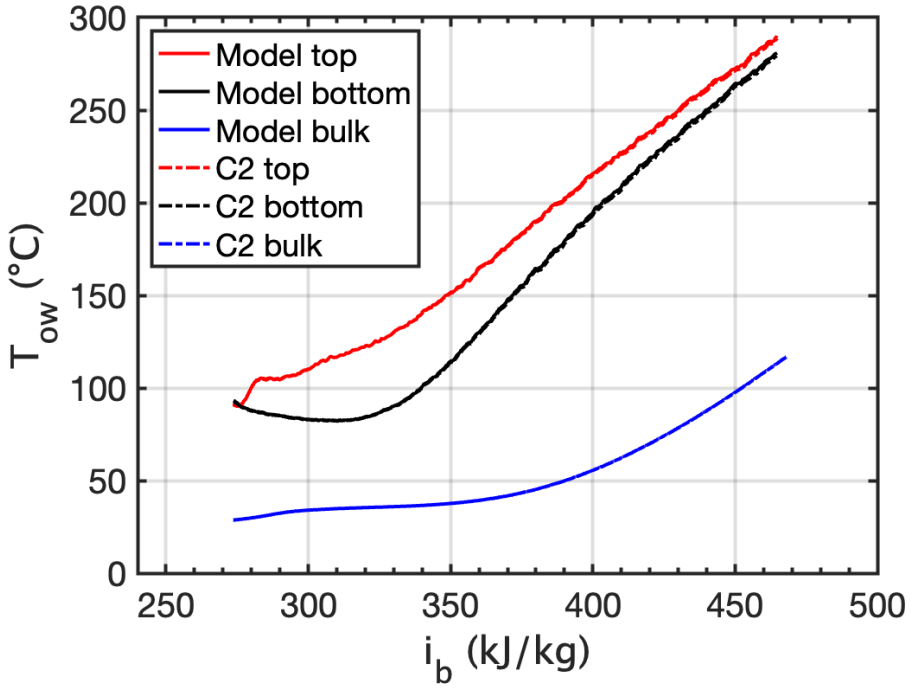

Figure B.3: Temperature profile for changing the value of $C_{2\epsilon}$

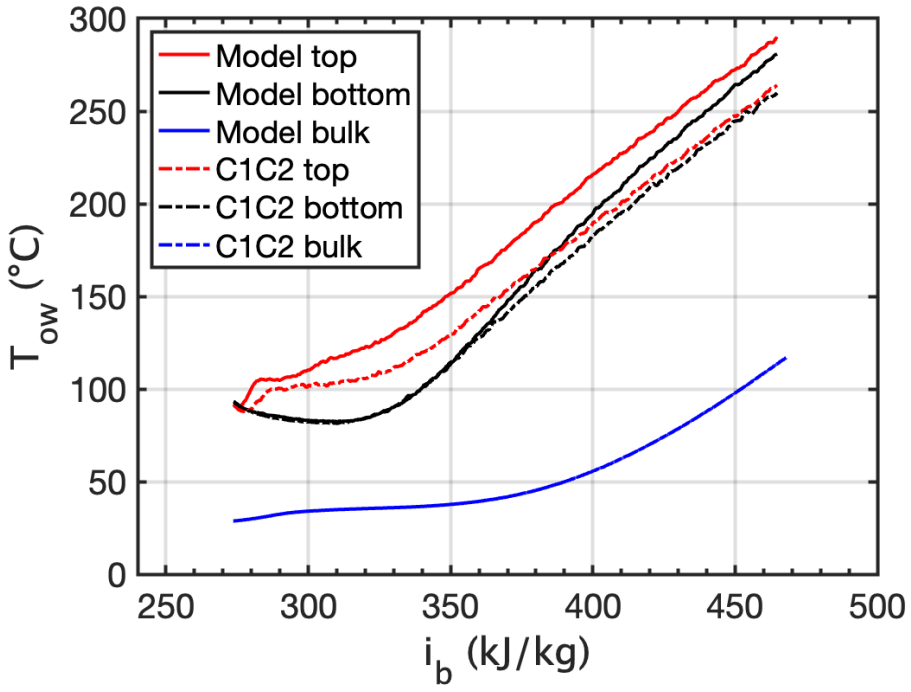

Figure B.4: Temperature profile for changing the value of both $C_{1\epsilon}$ and $C_{2\epsilon}$

C Dimensionless Numbers Feasibility Study

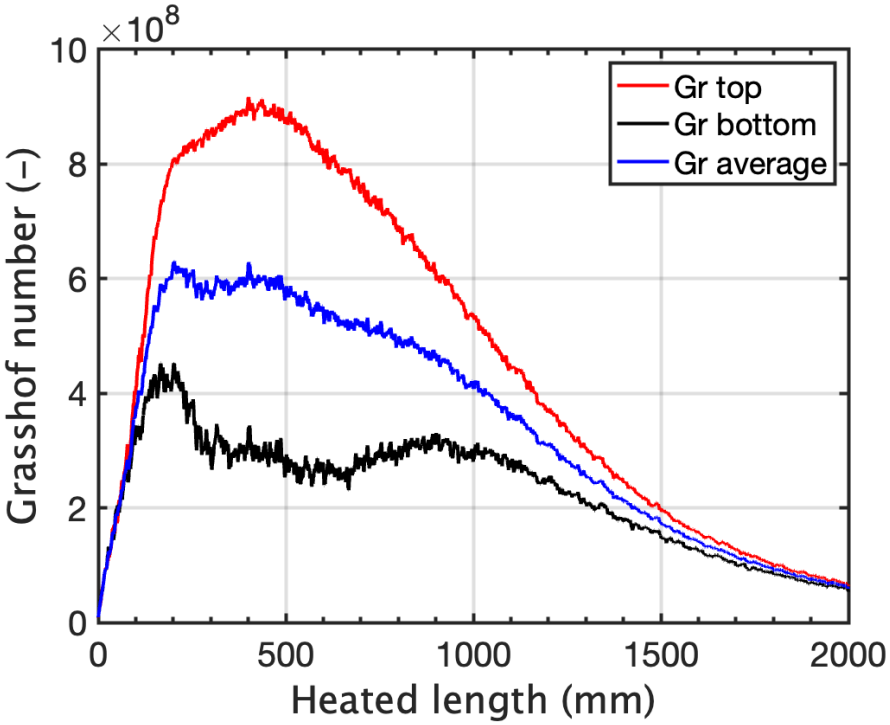

Figure C.1: Grashof number over the heated length for the feasibility geometry.

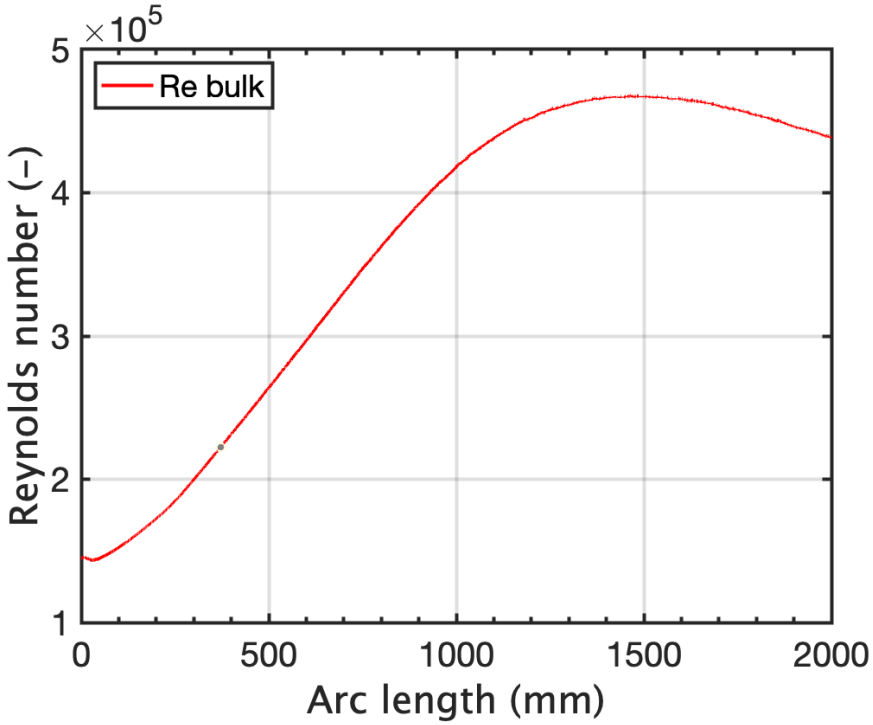

Figure C.2: Reynolds number over the heated length for the feasibility geometry.

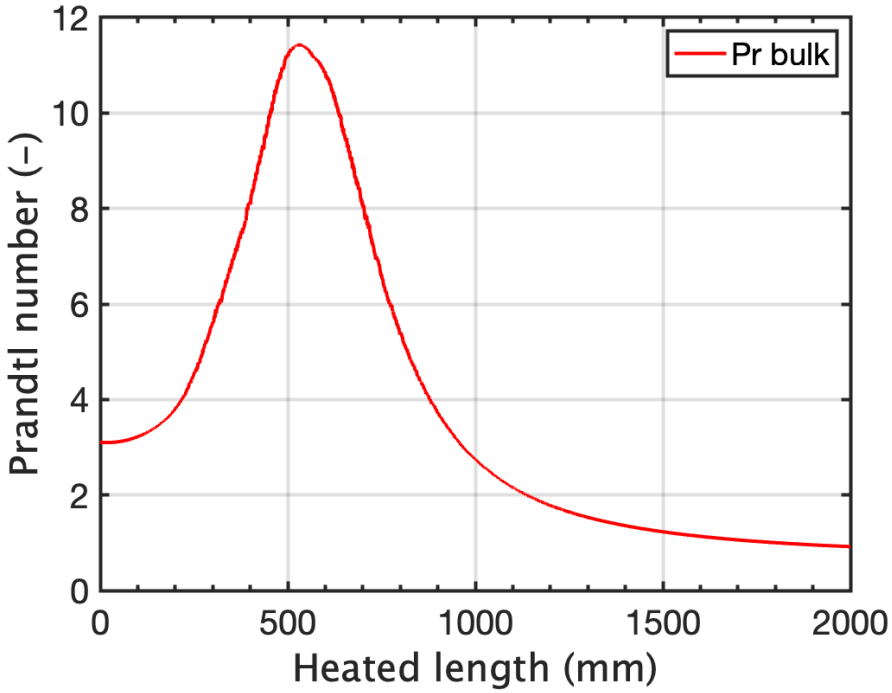

Figure C.3: Prandtl number over the heated length for the feasibility geometry.

D Dimensionless Numbers Monoblock

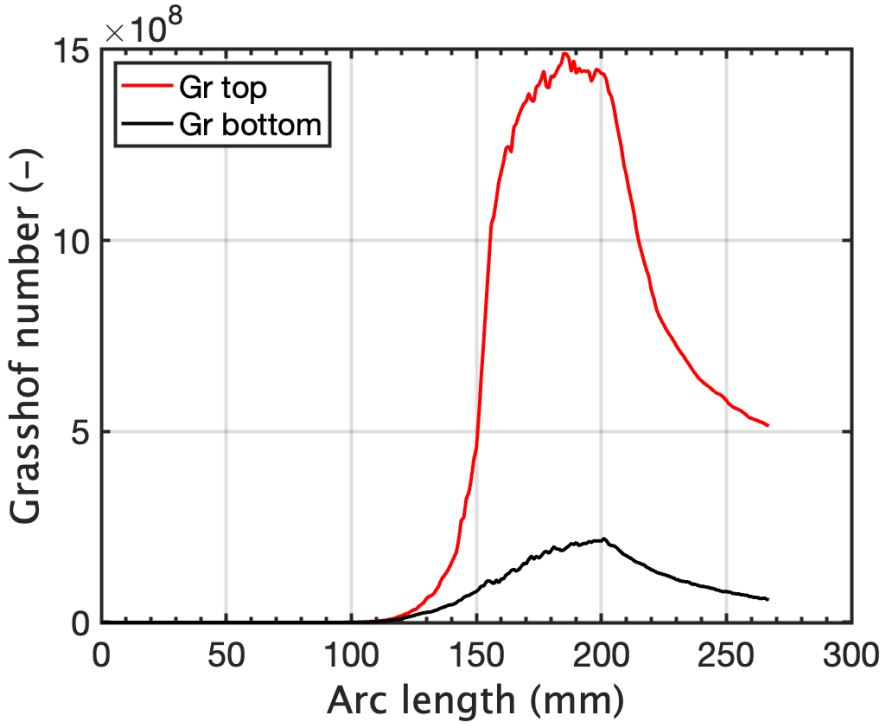

Figure D.1: Grashof number for the monoblock geometry for the 10 MW/m^2 case

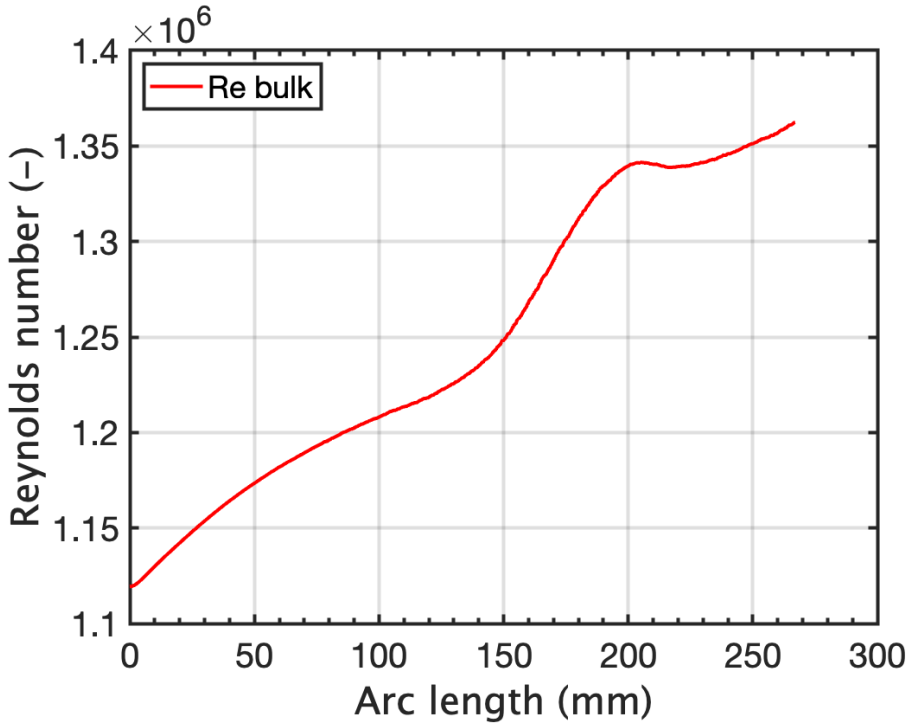

Figure D.2: Reynolds number for the monoblock geometry for the 10 MW/m^2 case

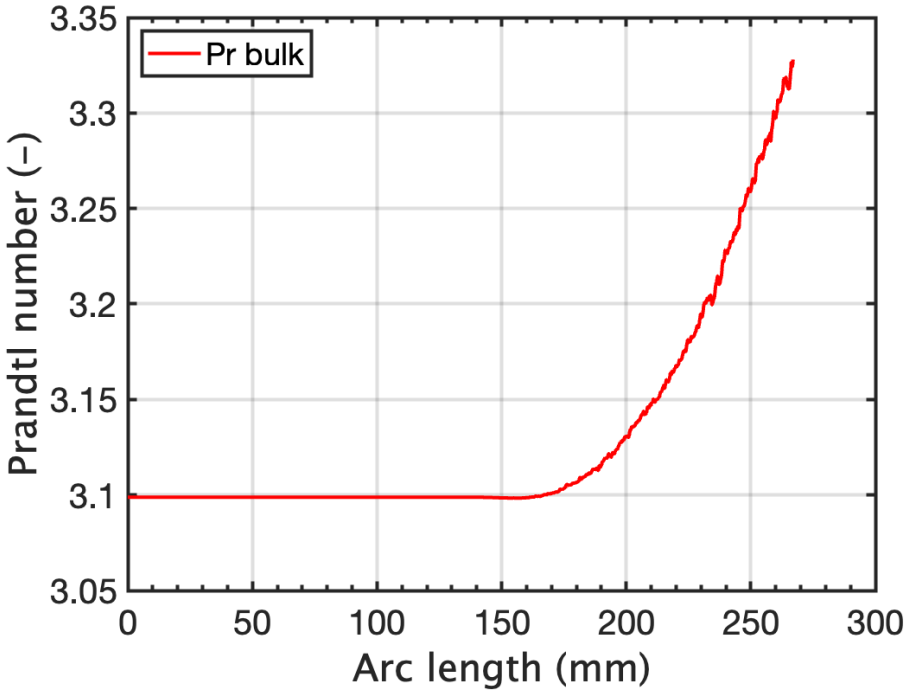

Figure D.3: Prandtl number for the monoblock geometry for the 10 MW/m^2 case

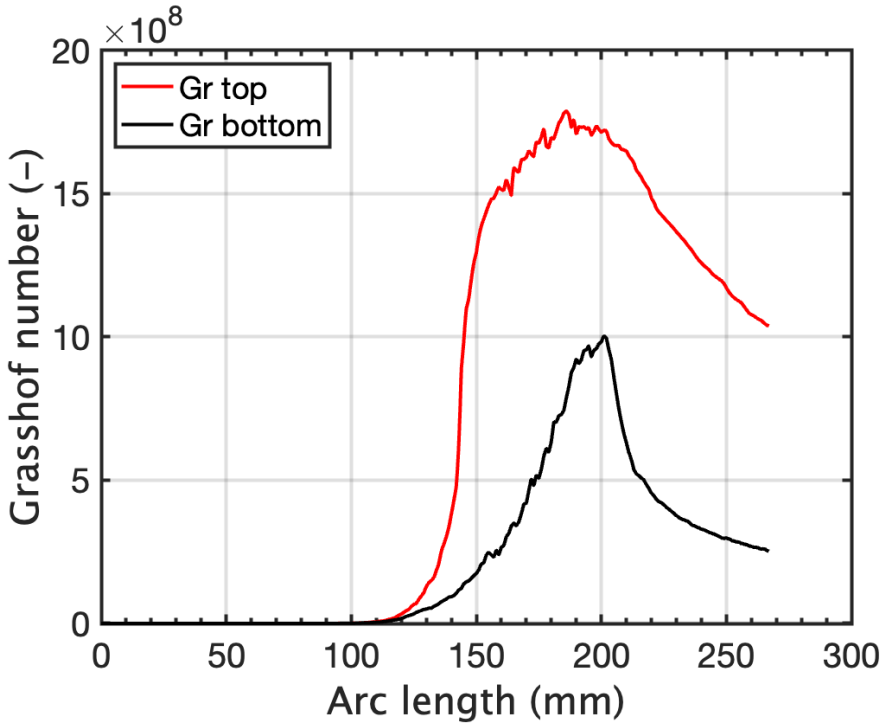

Figure D.4: Grashof number for the monoblock geometry for the 20 MW/m^2 case

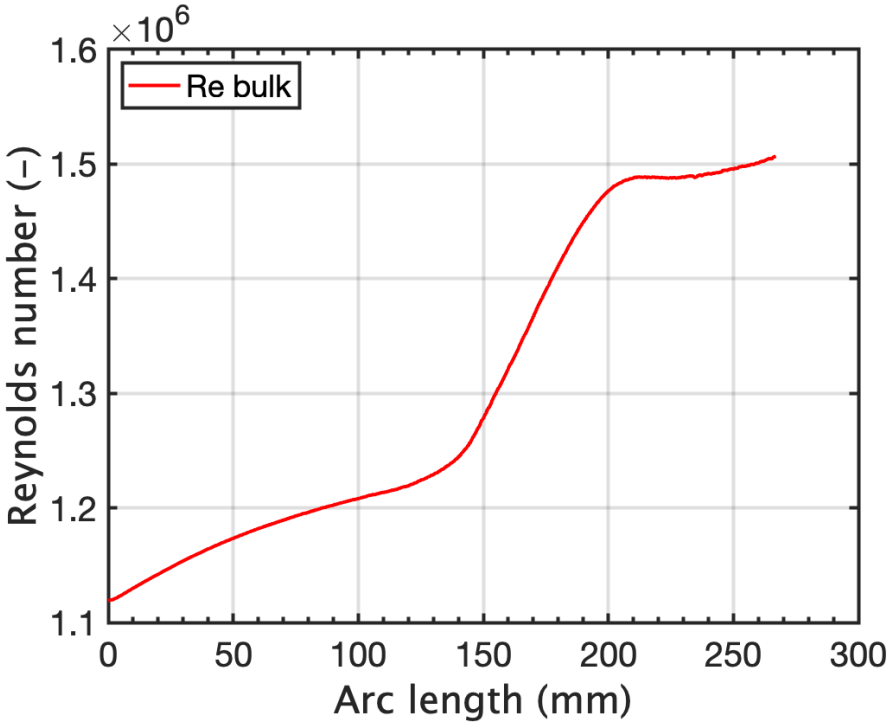

Figure D.5: Reynolds number for the monoblock geometry for the 20 MW/m^2 case

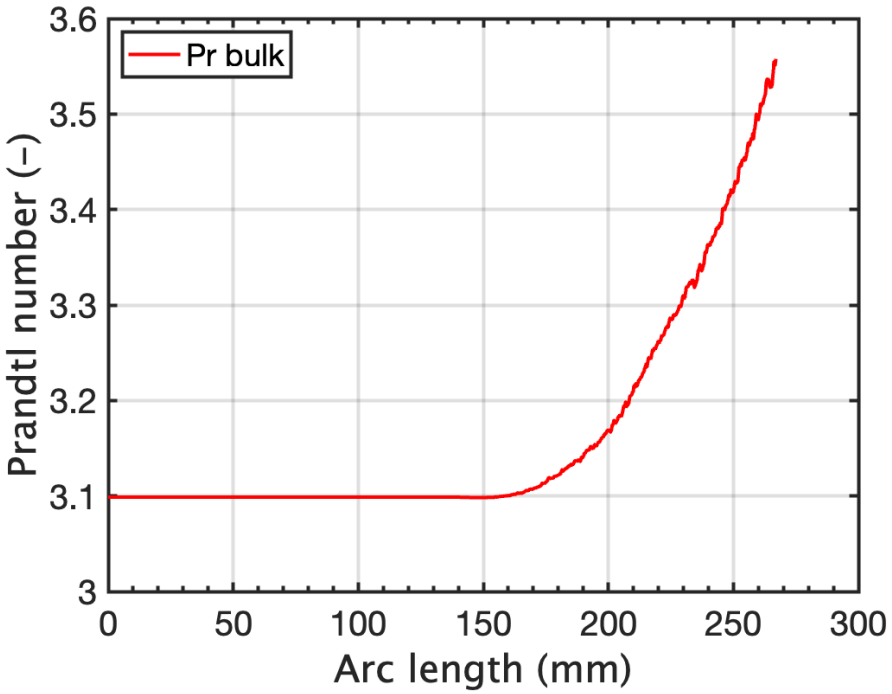

Figure D.6: Prandtl number for the monoblock geometry for the 20 MW/m^2 case